DEVELOPMENT OF A MICRO-FINITE ELEMENT MODEL OF THE INTERLAMELLAR MATRIX OF THE INTERVERTEBRAL DISC

ISKA PRETORIUS

MEB – MASTERS OF ENGINEERING (BIOMEDICAL)

FLINDERS UNIVERSITY

COLLEGE OF SCIENCE AND ENGINEERING

OCTOBER 2017

Table of Contents

Abstract

The annulus fibrosis (AF), within the intervertebral disc (IVD), is a heterogenous structure made up of various substructures. One such substructure is the inter-lamellar matrix (ILM), which is located between adjacent lamellae. It is theorized that the ILM plays a significant role in preventing delamination. However, limited literature exists on the exact function and mechanical properties of the ILM, in isolation. Therefore, micro-finite element models were developed representing the ILM, that were validated using experimental results. Three model types were developed: an ideal model, ideal model with an additional diagonal fibre, and a model of a partially digested ovine sample. The aim of the study was to initially develop a model of the ILM, validate the model, and then gain an understanding of how the fibre orientations within the ILM contribute to its mechanics.

Mechanical testing (unpublished) was conducted in shear and tension, on partially digested ovine ILM samples (Tavakoli et al., 2017a). The experiment was displacement controlled, during which the applied load and mechanical properties of the tested sample were measured. The experimentally applied load was used to validate the developed ideal model, after which the parameters used, such as the geometry and mechanical properties, were applied to the two remaining models. The ideal model was the reference model, from which the effects of fibre orientation variation, between models, could be studied.

It was determined that fibres orientated closer to the direction of the applied displacement, resisted the deformation more than the other fibres in the system. Under tension, along the x-direction, fibres orientated closer to the x-axis had a higher computational applied load, indicating that the fibres supported the applied displacement better in the x-direction. In shear, along the y-direction, fibres orientated further from the x-axis had a higher computational applied load, indicating that the fibres supported the applied displacement better in the y-direction. However, an increase in the computational load also increased the stress within the system and could therefore be a potential cause of initial fibre failure, which leads to failure propagation and finally delamination. It was also determined that an increase in fibre concentration attachment points, within an area, caused peak stresses within the system – with constant applied strain. Therefore, an increase in the amount of fibres attached to an area on the lamellae, could potentially cause failure such as fibre pull-out.

Declaration

I certify that this thesis does not incorporate without acknowledgment any material previously submitted for a degree or diploma in any university; and that to the best of my knowledge and belief it does not contain any material previously published or written by another person except where due reference is made in the text.

16/10/17

Iska Pretorius

Date

Acknowledgements

I would first like to express my gratitude to my thesis supervisor John Costi, for being an immense help throughout the entire master thesis process. I have learned an exceptional amount, especially from my mistakes – as you do not learn from doing things right – which is exactly what I wanted to gain throughout thesis.

I would also like to thank Mark Taylor, for making the time and helping me further understand finite element methods.

Furthermore, I would like to give a huge thank you to Javad Tavakoli for supplying incredible images, experimental results, and for always making time to help and explain everything in perfect detail. Without his help, I would truly have been lost.

Last but not least, I would like to extend a huge thank you to my partner, friends and family for being incredible supports throughout the entire process, especially my parents – I would not have achieved all that I have if it was not for them, they are my inspiration.

List of Figures

List of Tables

Chapter 1: Introduction

The intervertebral disc (IVD) is a fibrocartilage and lies between the vertebral bodies, located in the spine. It consists of two primary substructures, that are capable of withstanding complex loads: the nucleus pulposus (NP), and annulus fibrosis (AF) (Mengoni et al., 2013; Nerurkar et al., 2011). The AF consists of a very complex heterogenous structure, which enables it to withstand complex loads such as tensile, compressive, shear, and hydrostatic loads (Bruehlmann et al., 2002; Han et al., 2015; Mengoni et al., 2013; Michalek et al., 2009). The AF has its own substructures, that include: lamellae layers; collagen bundles, located within the lamellae layers; translamellar bridges, spanning across the entirety of the annulus fibrosis; and, the interlamellar matrix (ILM), located between the lamellae layers. The ILM consists of elastic fibres that are orientated at approximately ±45° and 0° relative to the lamellae, which include thick fibres ranging between 1 to 2 μm and thin fibres of approximately 0.1 μm (Tavakoli & Costi, 2016).

Disc degeneration, repetitive loading, and weak interlamellar connections are believed to play a significant role in causing disc herniation (Michalek et al., 2009). However, it is believed that the translamellar bridges and the ILM play a significant role in preventing delamination, which ultimately leads herniation (Smith et al., 2008). There is a major literature gap in understanding the function and mechanical properties of the ILM. The function of the ILM has been described through theories based on experiments conducted on the surrounding lamellae, giving an idea of its function. However, insufficient studies have been conducted on the ILM in isolation.

The aim of this study consisted of three parts: development of a micro-finite element model of the ILM, validation of the model, and understanding the influence of fibre orientation within the ILM. The first stage consisted of developing a model of the ILM, which was conducted in Matlab (The MathWorks, R2016a). The second stage comprised of validating the model, by comparing the computational output with the experimental results. Mechanical testing was conducted on various ILM samples, whereby all testing was displacement controlled under shear and tension (Tavakoli et al., 2017a). The experimentally applied load was measured during testing, which was used to validate the developed ILM ideal model. The parameters used in the validated model were applied to

two other developed models, that had different fibre arrangements, therefore the third aim was achieved and an understanding was gained of how varying fibre orientation contributes to the mechanics of the ILM.

Three model types were developed. An ideal model with fibres orientated at ±45°, relative to the x-axis, which was validated and used as a reference model. An identical ideal model with an additional diagonal fibre, which represented a fibre that was orientated over 45°, relative to the x-axis. Lastly, a model developed from an image captured of a partially digested ILM ovine specimen, which represented fibres orientated similarly to the biological system.

It was determined that fibres orientated along the applied displacement, better support the system. Therefore, under tension along the x-direction, fibres orientated closer to the x-axis supported the applied displacement better, due to the determined computational applied load increasing in the x-direction. In shear, along the y-direction, fibres orientated further from the x-axis supported the applied displacement better, which was evident by an increase in the computational applied load in the y-direction. An increase in the computationally determined applied load also increased the stress within the model, therefore fibres aligned with the applied displacement could cause initial fibre failure, leading to failure propagation, and ultimately delamination. It was also determined that an increase in the amount of fibres attached to an area, caused peak stresses within the system. Therefore, an increase in the amount of fibres attached to an area on the lamellae, could be a potential cause of failure, such as fibre pull-out. However, the quantity of fibres that would ultimately lead to failure needs to be investigated further.

Chapter 2: Literature Review

2.1 Background

The intervertebral disc (IVD) is a fibrocartilage that lies between the vertebral bodies, located in the spine (Nerurkar et al., 2010). The IVD is permanently loaded and therefore contains two primary substructures that are capable of withstanding and recovering from complex loads (Mengoni et al., 2013; Nerurkar et al., 2011). It consists of the nucleus pulposus (NP), located at centre of the disc; the annulus fibrosis (AF), which surrounds the NP; and an endplate, which lies between the disc and the vertebral bodies (Figure 1) (Nerurkar et al., 2010). The AF acts as an anchor keeping the disc attached to the vertebral body, which allows the spine to remain stable yet flexible (Yu et al., 2015).

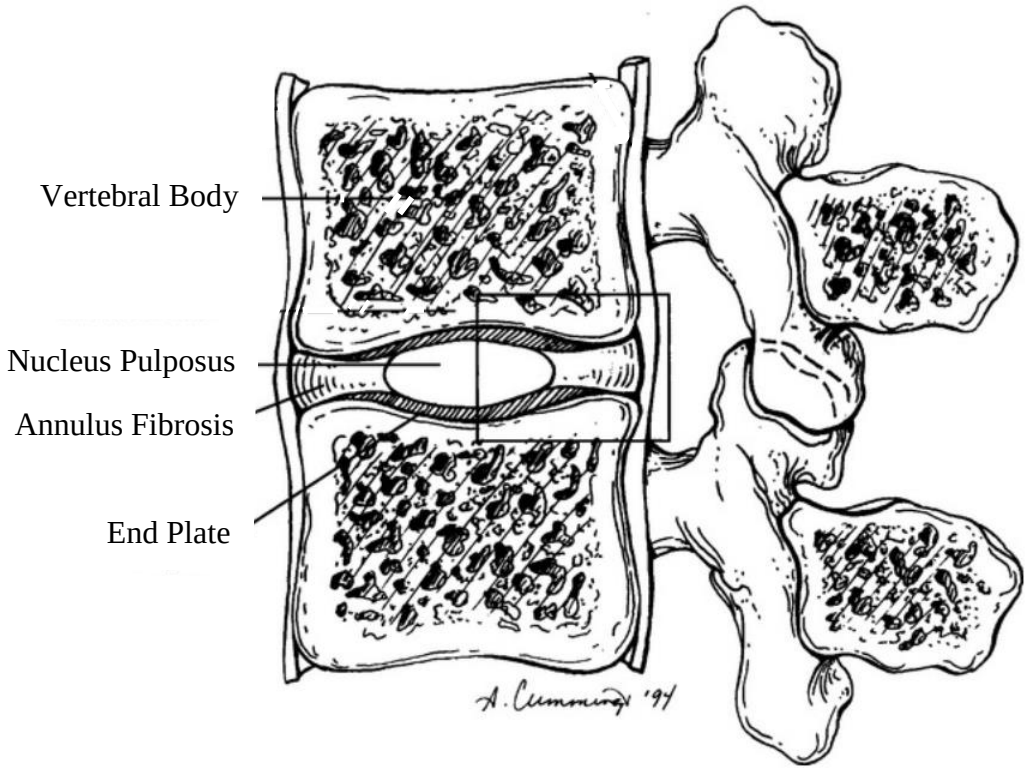

Figure 1. Structure of a motion segment from the spine, showing the vertebral bodies, nucleus pulposus, annulus fibrosis, and the end plate (Cramer et al.).

The AF is an intricate and heterogeneous structure, which requires properties that allow it to withstand multidirectional loads (e.g. tensile, compressive, shear, and hydrostatic loads) (Bruehlmann et al., 2002; Han et al., 2015; Mengoni et al., 2013; Michalek et al., 2009). As a result, the AF has complex mechanical behaviour, which is crucial for spine mechanics and ensures that it can endure severe as well as repeated loading during

everyday life (Vergari et al., 2016). The AF also constrains the radial bulge of the NP, allowing even distribution and transfer of loads between the vertebral bodies (Smith & Fazzalari, 2009). Therefore, the IVD has a highly intricate tissue structure enabling it to maintain its shape, health and function (Bruehlmann et al., 2002; Michalek et al., 2009). The major constituents of the AF are: collagen; proteoglycans; and elastin, a component that makes up elastic fibres. Collagen, which has the highest dry weight, consists of type I and type II collagen, where the concentration of type I collagen increases closer to the periphery of the AF (Han et al., 2015; Michalek et al., 2009). Proteoglycans, mainly aggrecan, is the second greatest in dry weight and contributes to the viscoelastic behaviour of the AF by attracting and preventing water movement (Michalek et al., 2009). Elastic fibres comprise of approximately 2% in dry weight and are resilient, linearly elastic, have high extensibility (Michalek et al., 2009), and play an important role in the AF – with the aid of collagen, proteoglycans and water (Smith & Fazzalari, 2009). Structurally, the AF contains highly aligned bundles within each lamellae layer, made up of collagen type I fibres that are surrounded by a proteoglycan-rich ground matrix (Labus et al., 2014), and are the main tension-bearing component within the AF (Nerurkar et al., 2010). The bundles have an alternating orientation either side of the transverse axis, of approximately 30°, and are arranged concentrically surrounding the NP (Figure 2) (Nerurkar et al., 2010; Smith et al., 2008; Smith & Fazzalari, 2009).

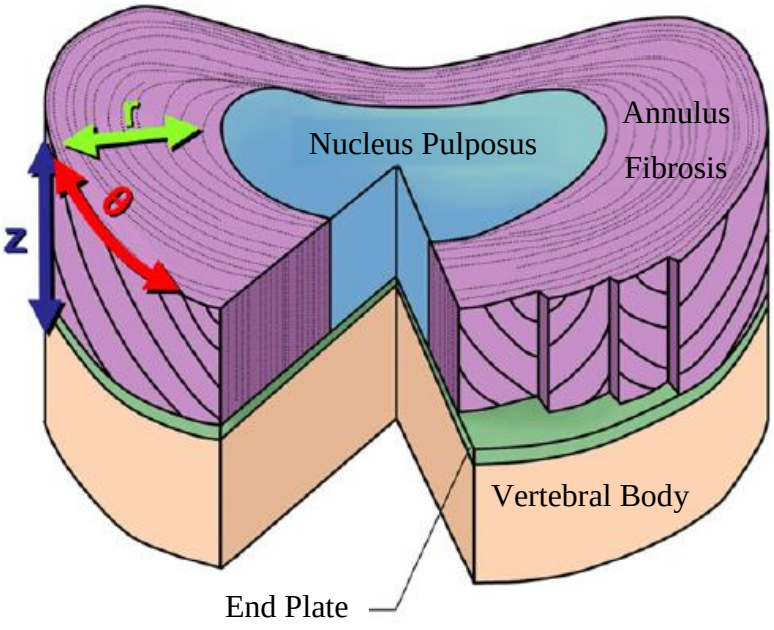

Figure 2. Multi-scale architecture of the intervertebral disc, showing the alternating orientation of the bundles with varying lamellae layer (Nerurkar et al., 2010).

Although numerous studies have been undertaken regarding the IVD, it is still considered a challenge to restore its function during and after degeneration (Nerurkar et al., 2010). Therefore, it is important to continue studying the various components of the IVD to better understand how it functions, in order to ensure that tissue engineering can closely replicate the properties of a physiological disc. Two methods previously used to relieve back pain, caused by disc degeneration, consist of fusion surgery and total disc replacement (Nerurkar et al., 2010). During fusion surgery, the vertebral bodies are fused together to prevent movement. Unfortunately, it has been found that over time fusion surgery does not cure pain and causes disc degeneration to occur, by increasing the wear rate of surrounding vertebral bodies (Nerurkar et al., 2010). Total disc replacement is a method whereby the disc is substituted with an artificial medical device and aims to maintain some mobility after disc replacement, however, device lifespan and mechanical wear have become major issues (Nerurkar et al., 2010). Consequently, current surgical implant solutions to replace the disc, try to stop the degeneration process, instead of attempting to repair the tissue (Labus et al., 2014). Therefore, more of an understanding of the intervertebral disc is required to aid tissue engineering to better mimic the physiological system.

During disc degeneration, the function of the elastin is believed to change. During age related degeneration, there is an increase in elastin, in terms of dry weight, and a noticeable decrease in elastic fibres that are still intact (Michalek et al., 2009). This indicates that the breakdown and synthesis of the elastic fibres may be part of a remodelling process (Michalek et al., 2009). It has been revealed that with an increase of elastin concentration, or an increase of the enzyme that synthesises elastin, that there is an increase in disc prolapse frequency (Michalek et al., 2009). It is believed that disc degeneration can be linked to: mechanical damage within the disc; loss of nutritional pathways or supply; and, biological degradation (Iatridis & ap Gwynn, 2004). Mechanical damage accumulation is believed to be the main difference between changes occurring within the disc due to degeneration and age-related changes, respectively. Understanding the causes of mechanical damage occurring, within the disc, will give insight into damage propagation and the difference between mechanical damage and biological degradation (Iatridis & ap Gwynn, 2004).

2.2 Annulus Fibrosis

Shear is an important loading direction within the AF and takes place during bending and torsion (Michalek et al., 2009). The maximum shear strain, believed to be a possible cause of failure, is at a maximum during the physiological movements: flexion-extension and lateral bending (Michalek et al., 2009). In fibre reinforced composite materials, shear causes microscale failure initiation and it is believed that a similar phenomenon occurs during the failure of the AF (Michalek et al., 2009). A difference in shear moduli was observed in ovine specimens, depending on the location within the AF, where there was an increase in stiffness in the outer anterior region, compared to that of the inner anterior (Labus et al., 2014). A similar difference was determined in another study, using ovine specimens, whereby the outer annulus had a significantly higher modulus than the inner annulus (Mengoni et al., 2015). This difference is believed to be due to the varying composition of the AF, whereby the outer AF has higher collagen content and the inner AF has higher glycosaminoglycan (GAG) content. A change in collagen fibre orientation has also been noted within the AF, another likely cause for the change in stiffness with varying depth (Labus et al., 2014).

The mechanics of the AF is highly intricate, making it a challenge to replicate and fully understand the multi-scale architecture that differentiates the AF from other soft tissues (Nerurkar et al., 2010). It was determined, within human tissue, that the interlamellar properties of the disc are important, to better understand the mechanics of the AF at the macroscopic level (Nerurkar et al., 2010). This further emphasises the need to fully understand the structures of the AF, at varying scales. An improved understanding of the AF, at varying scales, will add to the current knowledge of the AF mechanics, improve pain management, and give insight to tissue engineering.

2.3 Elastic Fibres

Numerous studies have been conducted on the AF, ranging from its over-all structural architecture to the variations at the cellular level (Mengoni et al., 2015; Smith & Fazzalari, 2009; Tavakoli & Costi, 2016; Tavakoli et al., 2017b; Yu et al., 2015). One such study, studied the elastic network of the AF within bovine samples (Yu et al., 2015). The study found that there is mechanical adhesion within and between each lamellae layer, at the interlamellar junctions (Yu et al., 2015). It is theorised that this mechanical

adhesion, which consists of a diffusing elastic network, is a mechanism that allows relative movement between lamellae layers and helps to restore the system from deformation (Yu et al., 2015). Within the human lumbar AF, the elastic network consists of: mature elastic fibres; elaunin fibres, that contain reduced elastin content when compared to the micro-fibrillar component; and oxytalan fibres, that fully consist of micro-fibrils and have no elastin component (Smith & Fazzalari, 2009). Although, elaunin and oxytalan fibres can function as fully developed fibres, they may also appear at the early stages of elastic fibre development (Smith & Fazzalari, 2009). The diameter of elastic fibres range between 0.2 – 1.5 μm, where the fibres are usually twisted or straight, and become effective in tension only (Mengoni et al., 2015; Tavakoli & Costi, 2016). The composition of elastic fibres generally consist of two segments: a central core, made up of amorphous elastin; and meshwork surrounding the core, made up of micro-fibrils (Tavakoli et al., 2017b). Therefore, the term "elastic fibres" will comprise of all three fibre types.

The elastic fibres play a significant and unique role in the mechanical properties of the AF, within human tissue (Smith et al., 2008), which is due to elastic fibres having a highly organised structure, that vary in distribution and orientation in different locations within the AF (Tavakoli & Costi, 2016). Therefore, by understanding the mechanical properties of the elastic fibres and its function in the AF will aid in its modelling, therapeutic targets, and tissue engineering (Smith et al., 2008). Generating models of the elastic fibres will aid in predicting mechanical damage within the system, adding to how the elastic fibres contribute to the entirety of the system (Smith et al., 2008). Therapeutic targets can be developed by understanding the source of potential pain or failure, which will aim to reduce discomfort and degeneration rate (Smith et al., 2008). Lastly, contribution to tissue engineering will be gained by adding to the understanding of the physiological system, from which synthetic or biological tissue replacements can be designed (Smith et al., 2008). Therefore, modelling elastic fibres and gaining an understanding of their function, would be valuable.

It has been determined that two distinct elastic fibre organizations exists within the AF (Tavakoli & Costi, 2016). Within the lamellae, elastic fibres are tightly packed within the surrounding matrix and align with the collagen fibres. Between two lamellae, or within the interlamellar compartment, the elastic fibres display a complex, dense, and

anisotropic arrangement (Tavakoli & Costi, 2016). Whereby, the elastic fibres between the lamellae layers were found to link the two interfaces, indicating that the elastic fibres could play an important role in preventing delamination – as the fibres seem to act as an adhesive between the adjacent lamellae (Smith et al., 2008). When comparing the elastic fibre arrangement seen within the lamellae and the interlamellar compartment, it has been noted that the concentration of elastic fibres is a great deal higher within the interlamellar compartment (Tavakoli & Costi, 2016). Within the collagen bundles, while loaded, some elastic fibres are in tension and others are slack, indicating that the collagen bundles can withstand loads applied in varying directions as different fibres are recruited with the change in direction (Smith et al., 2008). Therefore, the lamellae within the AF are anisotropic, consequently making the failure stresses and strains dependent on the direction of loading (Gregory et al., 2011).

The AF can be considered as a composite material, whereby its laminated structure prevents further failure by resisting crack propagation (Iatridis & ap Gwynn, 2004). Therefore, numerous cracks and micro-failures are required to allow the system to fully fail. Consequently, AF failure occurs by damage initiation, accumulation, and then final failure (Iatridis & ap Gwynn, 2004). The types of failures that exist within lamellae are caused by fibre failure and the propagation of fibre failure, whereby the following failure patterns exist: fibre pull-out, caused by longitudinal tension; matrix cracking, from transverse tension; and fibre buckling, caused by longitudinal compression (Iatridis & ap Gwynn, 2004). The fibres are the main structure within the lamellar layer supporting an applied load, for this reason the worst mode of failure occurs when multiple fibres fail, which could also lead to the failure of adjacent lamellae layers. It is therefore believed that both fibre failure and interlamellar stresses contribute to the failure of the AF (Iatridis & ap Gwynn, 2004).

2.4 Interlamellar Interactions

Interlamellar shear stresses and the delamination of lamellae layers within the AF, are a contributing factor to failure propagation (Goel et al., 1995; Iatridis & ap Gwynn, 2004). Whereby, high interlamellar shear stress, in conjunction with biological and chemical changes, may lead to the formation of cracks in the AF (Goel et al., 1995). It was also found that interlamellar shear stress is higher in the innermost posterolateral region within the AF and increases with the formation of radial or circumferential tears, or a

combination of the two. It has also been determined that minor changes to the length of circumferential cracks alter the interlamellar shear stresses by a greater magnitude (Goel et al., 1995). This relationship shows that cracks within the AF have a significant effect on the interlamellar shear stress. Within the AF, numerous failure patterns take place simultaneously caused by the composite laminate structure of the AF (Iatridis & ap Gwynn, 2004). Therefore, by altering the properties of the lamellae layers, caused by degeneration, increases the interlamellar shear stresses (Iatridis & ap Gwynn, 2004).

Few studies have been performed on the interlamellar interaction, although it is believed that weak interactions, between the lamellae layers, are a contributing factor to herniation (Michalek et al., 2009). It has also been shown that accounting for the interlamellar connectivity does output different stress and strain distribution, while the IVD undergoes physiological loading (Mengoni et al., 2015), indicating that the interlamellar interaction does have a significant contribution to the mechanical system. Herniation, or ruptures, are initiated by damage occurring within the AF and tears forming between collagen fibres within individual lamellae, leading to delamination or the propagation of cracks (Gregory et al., 2011; Vergari et al., 2016). Experimental studies have identified excessive shear stress between lamellae to be the primary cause of delamination (Gregory et al., 2011). Unfortunately, herniation is a common spinal disorder and is defined as a portion of the NP extruding through the layers of the AF or the endplates. This extrusion can cause the outer region of the AF to bulge and potentially press on the surrounding nerves, leading to debilitating pain (Gregory et al., 2011).

The main deformation occurring in the AF is proposed to be the sliding of the lamellae layers relative to one another, which has been reinforced by the ease of separating the layers through blunt dissection (Michalek et al., 2009). Radial deformation occurs, during load application, due to the separation of the lamellae layers and transverse bundle deformation (Smith et al., 2008). It has been determined that when the interlamellar interactions are ignored the comparison between the modelled system and the experimental system have a few discrepancies, demonstrating that the interactions or connections between these layers do in fact play a key role (Mengoni et al., 2015). Through peeling tests, it was determined that the lamellae in the outer superficial AF have a 30% higher peel strength, compared to that of the deeper outer region within the AF (Tavakoli et al., 2016). It was also found that the progression of delamination occurred

easier within the inner lamellae layers of the AF (Tavakoli et al., 2016). This indicates that a stronger connection exists between the lamellae layers with increased distance from the NP, with the strongest connections occurring at the outer region within the AF.

In porcine spines, it was determined that the interlamellar interface has a higher stiffness to that of the lamellae, whereby the lamellae underwent higher deformation than the interlamellar interface during tensile lap tests (Gregory et al., 2011). Although the behaviour of the interlamellar region has not been computationally modelled before, it has been determined that the computed interlamellar stiffness was constantly higher than the corresponding lamellar stiffness – indicating the complexity of the fibrous network within the interlamellar interface (Mengoni et al., 2015). A region of stress concentration was present at the exact location where the edges of the lamellae and interlamellar interface lap one another. Therefore, the shear stresses that resist debonding, or delamination, are concentrated at the region where the elastic fibres intercept the lamellae layer (Gregory et al., 2011). When a sliced segment of the AF from ovine, sectioned in line with the radial direction at 30° and 60 µm thick, undergoes a radial extension of 0.5 mm the lamellae undergo most of the deformation – where low levels of delamination was evident (Mengoni et al., 2015). Emphasising that the interlamellar region is stiffer than that of the lamellae layers. Although, limited studies have been conducted on the interface between lamellae layers, whereas studies have been done on individual lamellae (Michalek et al., 2009). It has been determined that the mechanics of the lamellae vary with the alterations of the: fibre orientation, fibre properties, matrix properties, and interaction between the matrix elements (Michalek et al., 2009).

The microscale deformation occurring within the AF, during transverse shear, is the result of interlamellar skewing and its magnitude is associated with the orientation of the lamellar layer, relative to the applied shear (Michalek et al., 2009). Under radial tension there is little to no sliding occurring between lamellae layers, indicating that a rigid fibrous connection exists between the boundaries preventing movement, opposed to friction (Michalek et al., 2009). However, it was determined that the elastic fibres, even at high concentration, do not have a significant effect on the boundary mechanics, while undergoing shear (Michalek et al., 2009). Therefore, the elastic fibres add to the rigidity or stiffness of the system, perpendicular to the lamellae layer. Fibre uncrimping and re-organisation occur simultaneously in the system, indicating that the interlamellar

connections are relatively rigid (Michalek et al., 2009). Consequently, transverse shear is believed to result in both sliding and skewing of the interlamellar layers, and circumferential shear is believed to result in stretching, uncrimping, and rotation of the collagen bundle fibres (Michalek et al., 2009).

The interlamellar shear strain is primarily caused by skewing and not sliding, where no sliding was observed between lamellae during tensile testing, in bovine specimen (Vergari et al., 2016). It was determined that the interlamellar linear strain was 3 times larger than that of the strain within the lamellae, indicating that there is rigid cohesion between lamellae (Vergari et al., 2016). The difference in strain is believed to be caused by two mechanisms that allow slight shifting, the movement of lamellae relative to one another and fibre bundle movement relative to one another (Vergari et al., 2016). It was found that the bundles, within the lamellae, remained parallel to one another even while undergoing sliding and rotating. Therefore the mechanical role of the inter-bundle connections is to allow slight movement between bundles (Vergari et al., 2016). This mobility reduces as the number and stiffness of the elastin cross-bridges increases, and the bundle interconnection increases – both of which take place with aging (Vergari et al., 2016).

2.5 Translamellar Cross-Bridges

A secondary structure exists within the AF called translamellar cross-bridges, that are rich in elastin and collagen type VI (Han et al., 2015) (Figure 3). Another study identified collagen type I as an additional component making up the cross-bridges, within ovine specimen (Schollum et al., 2008). The bridging structures usually transverse through twelve, or more, lamellae at a time within a single 30 μm thick oblique slice, in ovine specimen (Schollum et al., 2009). The collagen component is responsible for the strength and stiffness of the cross-bridges and prevents slipping between adjacent lamellae (Schollum et al., 2008), where it is been described that torsion, flexion, and extension cause slipping between adjacent lamellae (Schollum et al., 2009). Slipping is prevented by the mechanical behaviour of collagen, which has a J-shaped stress-strain response. Therefore, once the collagen has achieved its initial crimp straightening stage, it will stiffen quickly and prevent further movement (Schollum et al., 2008). The elastin rich component is believed to have a supportive role within the cross-bridges, where it could likely help restore the collagen crimp under very low stress (Schollum et al., 2008).

It is believed that the formation of these cross-bridges is caused by the vascular regression which takes place during the growing and maturation stages of the postnatal years (Han et al., 2015). Vascular regression, in this case, is caused by the reduced metabolic requirements and the mechanical stress surrounding the matrix (Han et al., 2015). It is thought that the penetrating blood vessels, that regress, do not become a part of the lamellar region and rather form structures similar to that found in the interlamellar compartment, or the interlamellar matrix (ILM). Thus, forming the translamellar bridging structures, or translamellar cross-bridges (Han et al., 2015).

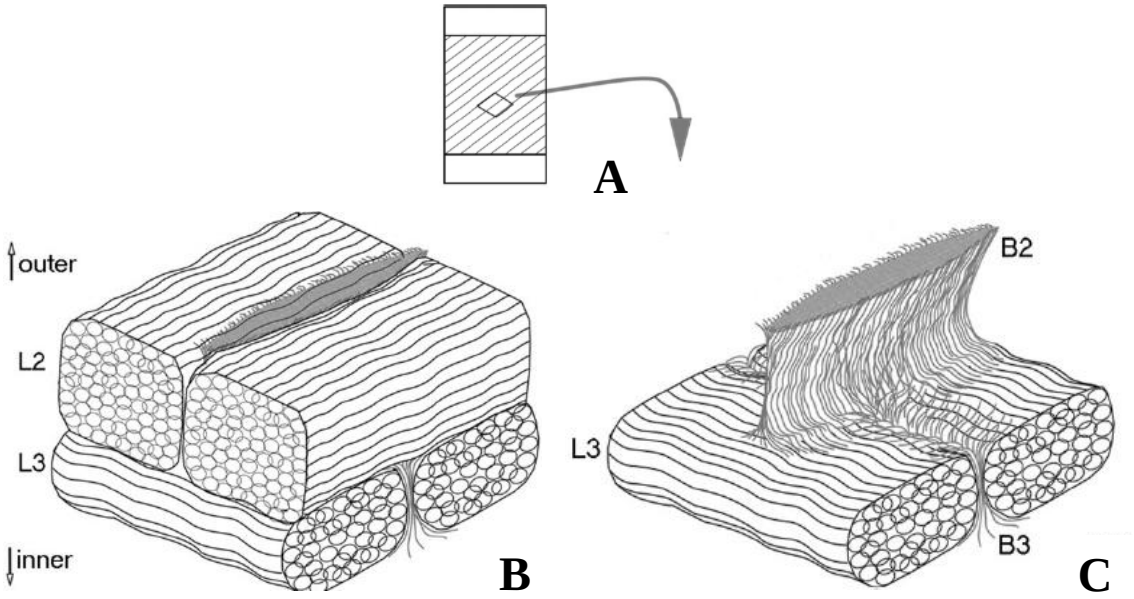

Figure 3. Proposed fibrous model for the translamellar bridges, representing two layers of lamellae. (A) Cross-section of the intervertebral disc, from which a section has been taken and enlarged, denoted by the square-like outline. (B) Two layers of lamellae, L2 and L3, consisting of two bundles each. (C) One lamellae layer removed, L2, to reveal the proposed cross-bridge fibrous structure, B2 and B3 (Schollum et al., 2009).

Cross-bridges can be identified as a distinguishable structure that are situated between collagen bundles, within lamellae, and weave through various lamellae in the radial direction (Han et al., 2015; Labus et al., 2014). It has been observed that cross-bridges, within ovine samples, are anchored into adjacent and non-adjacent lamellae, securing the lamellae layers (Schollum et al., 2008). It is believed that the alternating fibre orientation of the cross-bridges may be a contributing factor to the high interlamellar shear that takes place during physiological loading. Therefore, adding to the over-all stiffness of the AF,

within ovine specimen (Labus et al., 2014). Even though the bridging structures secure the lamellae, slight amount of interlamellar movement is still accommodated, allowing for minor deformation and normal function (Schollum et al., 2009). Although, not enough is known about cross-bridges to accurately determine its 3-dimensional structure or mechanical role. However, it is still believed that cross-bridges do affect local tissue deformation, due to its varying fibre orientation and structure compared to that found in the lamellar region (Han et al., 2015).

The extent of the translamellar bridging matrix, between the lamellae bundles, is relatively variable, indicating that the cross-bridges do not stay within a single bundle interface, but extend past this region (Han et al., 2015). The cross-bridges branch and weave between the highly aligned alternating lamellar architecture, into neighbouring inter-bundle spaces, making up a network of translamellar bridges (Schollum et al., 2008). It was found that the span of the translamellar bridging matrix ranged from 758 to 1,420 μm, within any given lamellae, where the layout and extent of the cross-bridges differ with varying lamellae layer (Han et al., 2015). The collagen fibres found in cross-bridges differ in orientation to that found in the lamellae layer and tunnel through the lamellae in a radial direction, opposed to alternating at 30° (Han et al., 2015). It is believed that the structure and the radial orientation of the translamellar bridges play a key role in preventing delamination (Schollum et al., 2009).

2.6 Interlamellar Matrix

Between each lamellae layer, within ovine samples, a highly rich collagen and elastin compartment exists, known as the ILM, and is made up of a complex and rich network of fibres (Labus et al., 2014) (Figure 4). The ILM ranges between 20 to 30 μm thick, which is approximately one-eighth of the thickness of a single lamellae (Tavakoli et al., 2016). When comparing the fibre orientation between the intra-lamellar and ILM regions, within ovine specimen, it is noted that the intra-lamellar elastin and collagen fibres are aligned with one another, whereas the ILM elastin fibres are complex and appear to be unaligned (Tavakoli et al., 2017b). The ILM is made up of four major components, which includes matrix, cross-bridges, elastic fibres, and cells (Tavakoli et al., 2016). It has been noted that the cell types within the ILM varies to that found within lamellae, indicating that the ILM may have some biological activity and function independently to that of the lamellae (Labus et al., 2014).

The ILM has a different micromechanical environment to that of the translamellar cross-bridging matrix (Han et al., 2015). However, some characteristics are similar, where both contain higher levels of collagen type IV, proteoglycans, and elastin, relative to the matrix of the AF – which mainly consists of collagen type I and type II (Han et al., 2015). Varying opinions exist on the mechanical benefit and function of the ILM. Schollum et al. (2008) mentions that the irregular elastin mesh within the ILM is an unlikely contributing factor to the overall mechanical strength of the disc wall (Schollum et al., 2008). Whereas Gregory et al. (2011), states that the ILM plays an important role in preventing delamination or herniation between lamellae (Gregory et al., 2011). It has been determined that herniation occurrence is more likely to occur in the outer posterior part of the AF, caused by weak connections within the ILM (Tavakoli et al., 2016). Indicating that the quality of the ILM does influence the mechanical strength of the AF.

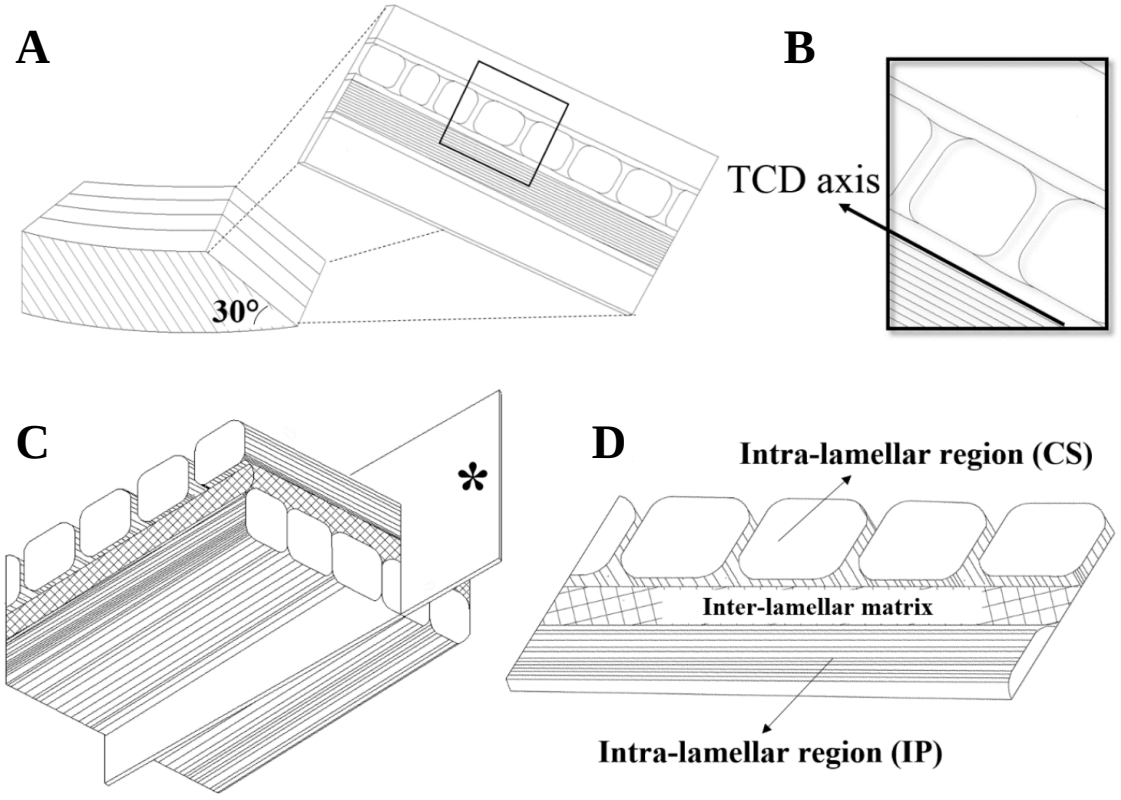

Figure 4: Showing the location of the ILM. (A) A section taken from the AF, cut at 30°, from which another section at 30 µm thickness has been taken, denoted by the square. (B) The direction of the tangential to the circumferential direction, TCD-axis. (C) Two lamellae layers, one in plane (IP) and another in cross-section (CS). (D) Two lamellae layers, between which the ILM is located (Tavakoli et al., 2017b)

The ILM is theorized to play a key role in returning the AF to its original shape after deformation, which is due to the presence of the highly extensible elastic fibres (Tavakoli et al., 2016). When elastic fibres are removed from the ILM it had a significant effect on the toe and linear region modulus (Tavakoli et al., 2016). Both the toe and linear region modulus decreases, 0.07 to 0.004 MPa and 0.21 to 0.02 MPa, respectively (Tavakoli et al., 2016). There was also an increase in the extensibility, 0.16 to 0.93 mm/mm, and a decrease in the AF radial tension (Tavakoli et al., 2016). Therefore, some evidence exists indicating that the ILM does play a significant role in the mechanics and strength of the AF. However, more studies are required to fully understand the true function of the ILM.

A study was conducted during which ovine lamellae underwent shear, where two types of specimens were tested: a single lamellae and a combination of a single lamellae with the ILM (Labus et al., 2014). Both specimen types had a non-linear stress-strain relationship, where the combined specimen had a greater strain than that of the individual lamellae specimen (Labus et al., 2014). The difference in strain was due to the lamellae layers sliding relative to one another with the presence of the ILM, and little movement taking place within the single lamellae specimen (Labus et al., 2014). The difference in strain is supported by the higher shear moduli determined for lamellae and the high deformations the ILM undergoes in vitro (Labus et al., 2014). Additionally, the difference in shear increased between the two specimen types in the outer anterior region within the AF and were almost equivalently at the inner anterior region. This indicates that the ILM possibly has more of a mechanical effect on the system in the outer region of the AF, which has been supported by other studies (Labus et al., 2014; Mengoni et al., 2015; Tavakoli et al., 2016).

Through the use of a digestion technique, to further understand the structure of the ILM, the surrounding matrix and collagen matter was removed from ovine specimen and images collected (Tavakoli et al., 2017b). Highly detailed images were collected, presenting the elastic matrix within the ILM at varying scales (Figure 5). By gaining a better visualization and understanding of the structure and of the ILM could potentially be highly beneficial in determining how it contributes to disc mechanical properties, integrity, and response to complex loading conditions (Tavakoli et al., 2017b). Further studying the ILM will add to the understanding of how stress is distributed within the AF, and give further insight into failure propagation (Tavakoli et al., 2017b).

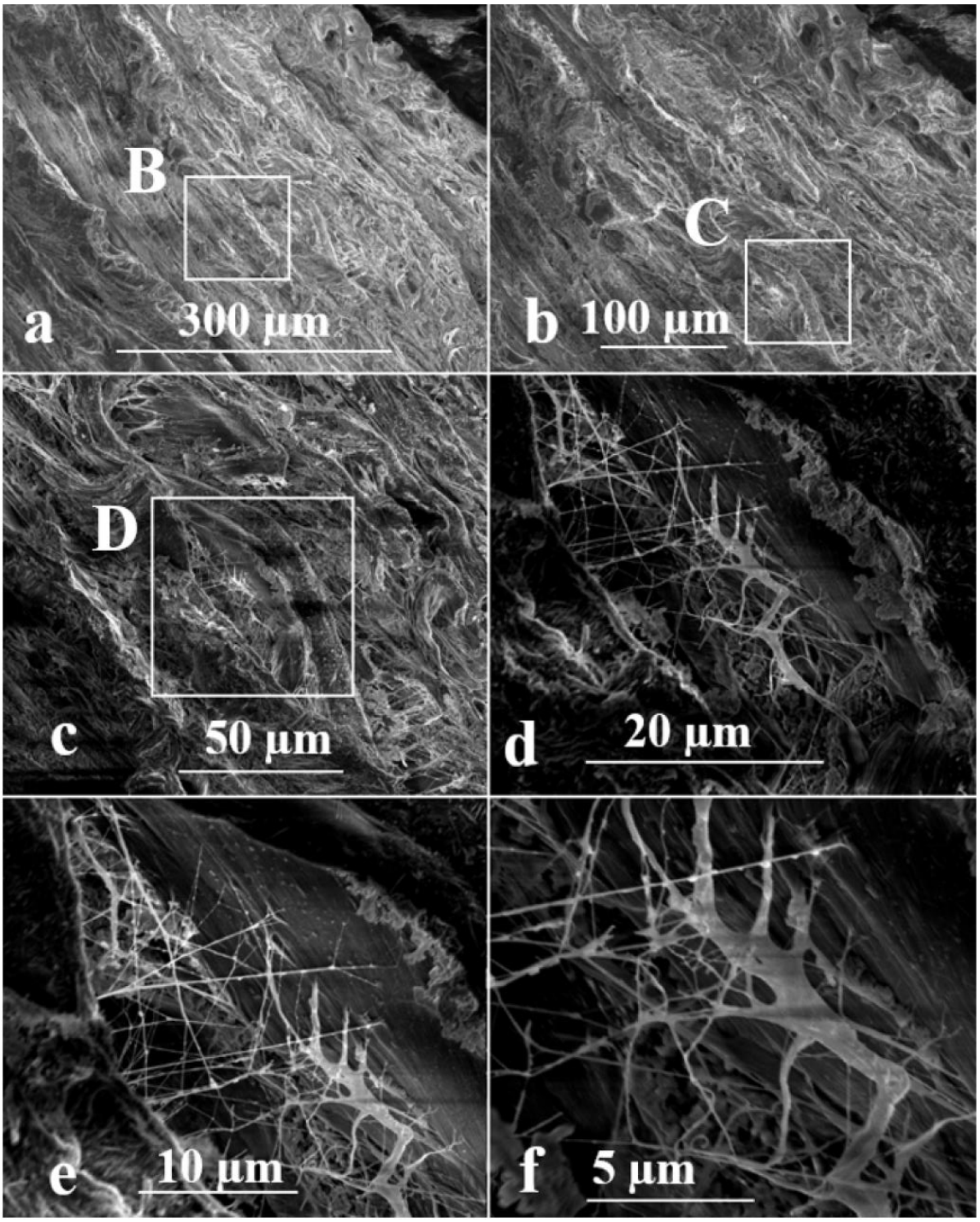

Figure 5. SEM images, showing the elastic structures of the ILM. (a, b) Low magnification, indicating the area from which the ILM structure was analysed, between two neighbouring lamellae. (c – f) Increasing magnification of the ILM, showing more details and revealing the complexity of the elastic fibre ultrastructure. (f) Fibre at approximately 0°, relative to the lamellae or TCD-axis. Boxes labelled as B, C, and D correspond to the higher magnification images b, c, and d, respectively (Tavakoli et al., 2017b).

In order to visualise the ILM, a magnification of 20 – 2,000× has to be used, whereby the scale of the output images range from 20 to 500 µm (Tavakoli et al., 2016). It was determined that the elastic fibres form a complex and dense network within the ILM, when compared to the intra-lamellar region (Tavakoli et al., 2017b). Elastic fibres were both thick and thin, where the thick fibres ranged between 1 to 2 µm and the thin fibres were approximately 0.1 µm. Two main methods of anchoring were noted when studying the images. The thinner elastic fibres connected by means of branching out and the thicker fibres merged directly into the intra-lamellar region, respectively (Tavakoli et al., 2017b). Although, the fibres seem as though they are randomly orientated, it was found that the angle of rotation was symmetrical (Tavakoli et al., 2017b). It was determined that, relative to the TCD axis, the fibres were orientated at about ±45° and 0° (Figure 4). Comparing the ratios of fibre orientation, it was determined that there was a greater quantity of fibres orientated at ±45° (Tavakoli et al., 2017b). In addition, the density of fibres within the ILM increased closer to the outer region of the AF and decreases closer to the NP (Tavakoli et al., 2016). Therefore, the ILM could be responsible for the increase in stiffness in the outer region of the AF.

It is theorised that the failure of the ILM causes delamination within the AF and could possibly take place during the early stages of final failure (Tavakoli et al., 2016). Delamination, tears, and the additional disc degeneration within the AF, are associated with the structural integrity of the ILM (Tavakoli et al., 2016). Therefore, by gaining more of an understanding of the ILM would give insight into: failure propagation; failure initiation; modes or causes of failure; failure loads; stress distribution; AF deformation under complex loads; and AF mechanical properties.

2.7 Finite Element Modelling

Finite element (FE) modelling is a useful method used to determine the physiological loading environment (Labus et al., 2014). However, the output of the model is highly dependent on what the user has input into the system. Therefore, there are two important parameters that need to represent the physiological system as closely as possible, the geometry and material properties (Labus et al., 2014). A model that was developed, derived from experimental results, assumed that the AF is a homogenous tissue that consisted of two main families of fibres – instead of representing the lamellae and ILM individually with the appropriate interactions (Labus et al., 2014). It was noted that the

assumption and description of the model was appropriate to model the global AF tissue behaviour, for various loading conditions (Labus et al., 2014). However, larger differences have been found between the experimental and the proposed model in the outer anterior region, indicating that there is a greater difference in stiffness in this region likely contributed by the ILM (Labus et al., 2014). Therefore, as previous studies have also found, the ILM has a greater effect on the AF mechanics closer to the outer region of the AF (Labus et al., 2014; Mengoni et al., 2015; Tavakoli et al., 2016).

A FE model was developed that represented a section of the AF consisting of a few lamellae layers, which was established by using the geometry and boundary conditions collected from experimentation, allowing the proposed model to be verified (Mengoni et al., 2015). However, it was found that the proposed model had consistently higher lamellar stiffness values (Mengoni et al., 2015), emphasising the complexity of the fibrous connections within the interlamellar interface, the details of which was omitted in the proposed FE model. The bridging structures may also affect the mechanics of the AF, whereby the bridging structures extent radially throughout the entire AF (Mengoni et al., 2015). Therefore, emphasising the need to understand how the fibres contribute to the mechanics of the AF. Pure collagen has an insignificant effect on the mechanical properties of the AF, however, it does have an effect on the biochemical changes (Smith et al., 2008). Demonstrating that the collagen, within the ILM, will likely have little to no effect on the mechanical properties of the AF.

2.8 Study Aim

The aim of this study consists of three parts. The first part, is to develop a model that closely resembles the ILM, using FE methods. The second part, is to validate the developed model by comparing the output of the model to experimental results. The third part, is to gain an understanding of how the fibres within the ILM contribute to the mechanics of the system, by using the developed and validated model.

Chapter 3: Methodology

3.1 Overview

The structure of the ILM was captured using a digestion technique and Scanning Electron Microscopy (SEM) (Figure 5) (Tavakoli et al., 2017b). The captured images from the study of Tavakoli et al. (2017b) were used to determine the orientation and distribution of the elastic fibres located in the ILM, and it was determined that the fibres were orientated at approximately ±45° and 0°, relative to the TCD axis (Figure 4) (Tavakoli et al., 2017b). However, reference will be made to the x-axis, whereby 0° becomes 90°.

Therefore, three 2-dimensional model types were developed:

(1) Ideal model (IM),

(2) Ideal model with a diagonal fibre (IMD), and

(3) Specimen model (SM)

3.1.1 Ideal Model

For the IM, fibres were orientated at ±45° relative to the x-axis. The IM represented the findings whereby fibres were orientated at ±45° within the ILM (Tavakoli et al., 2017b), and was used as a reference, to which the IMD and SM outputs were compared to.

3.1.2 Ideal Model with Diagonal Fibre

The IMD was a further development of the IM, which was developed with a diagonal fibre running from the bottom-left to top-right region, which represented a fibre at approximately 90°, relative to the x-axis. The additional fibre represents the third fibre orientation discovered in the SEM images, with fibres orientated at approximately 0°, relative to the TCD axis (Figure 4) (Tavakoli et al., 2017b). Although the diagonal fibre was not at 90°, relative to the x-axis, the reason such a fibre orientation was selected was to reduce model complexity, size and to account for the 90° fibre thickness. If a close to 90° fibre was added to the model the model height would have increased by a significant factor, due to the fibre having to connect to the left- and right-hand boundary – which would have increased computational time and model complexity. The fibre at 90° was also significantly thicker, therefore by increasing the fibre angle, relative to the y-axis, increased its contribution to the model. The developed IMD acted as the first step towards developing a model, which includes all three fibre orientations established in the ILM,

and insight was gained into how a fibre orientated at a more than 45° contributed to the system. The output of the IMD was compared to the IM output, through which it was possible to gain an understanding of how the diagonal fibre contributed to the mechanics of the ILM.

3.1.3 Specimen Model

A third and final model, SM, was developed by using an image captured of a partially digested ILM specimen (Figure 8). The final SM was compared to the output of the IM, to understand how the orientation of the fibres within a specimen contributes to the mechanics of the ILM.

3.1.4 Modelling Overview

Modelling was implemented using Matlab (The MathWorks, R2016a), where each fibre was represented as a spring. The aim was to validate the IM by comparing the output of the developed model with that of experimental results (unpublished) (Tavakoli et al., 2017a). After the model was validated, the parameters used in the IM were applied to the remaining two models, from which it was possible to gain an understanding of how the fibres contribute to the mechanics of the system.

3.2 Assumptions

Assumptions were made to reduce the complexity and computational time of the developed model, some of which were supported by other studies.

- Elastic fibres have uniform mechanical properties across the model.
- Elastic fibres are linearly elastic (Michalek et al., 2009; Smith & Fazzalari, 2009) and can therefore be modelled as springs.
- If there is a negative load within the elastic fibre, it is assumed to have zero load due to the fibres collapsing and will therefore have no effect or support within the system (i.e. the elastic fibre will be in compression).
- The lamellar boundary is flat.
- The elastic fibres are directly attached to the lamellar boundary, creating a vertical connection point parallel to the lamellar boundary.
- The lamellar boundary has a higher stiffness than the ILM, when digested, and therefore does not deform significantly under tension or shear.

- Collagen has little to no mechanical effect on the system and can therefore be omitted (Smith et al., 2008).
- The elastic fibres form an ideal adhesion to the lamellar boundary.
- The initial condition of all the elastic fibres are unstrained and uncrimped.
- All models are quasi-2-dimensional with a single layer of aligned elastic fibres.

3.3 Ideal Model Development

During the initial stages of model development, determining the geometry of the ILM was the first step, which consists of: the distance between adjacent fibres, ILM thickness, and fibre thickness. Adjacent fibre distances were determined from an image captured (Figure 8), from which the distance between fibre attachment points were measured and averaged. It was determined that the distance between adjacent fibres is approximately 2.3 μm (Appendix A). The ILM thickness, or the distance between the boundaries, for the IM and IMD, were taken as the average thickness of the ILM. The ILM ranges from 20 μm to 30 μm (Tavakoli et al., 2017b), therefore the ILM distance was taken as a value close to the average, 25.3 μm. The exact average of 25 μm was not used, because 25.3 μm is divisible by 2.3 μm, therefore allowing the IM and IMD to be uniform and symmetric, with fibres orientated at ±45° relative to the x-axis. The fibre thickness was determined as the average between the maximum and minimum fibre thickness found within the ILM, 0.1 μm and 2 μm (Tavakoli et al., 2017b), therefore the fibre thickness used in all the models was 1.05 μm. (Figure 6 and Figure 7)

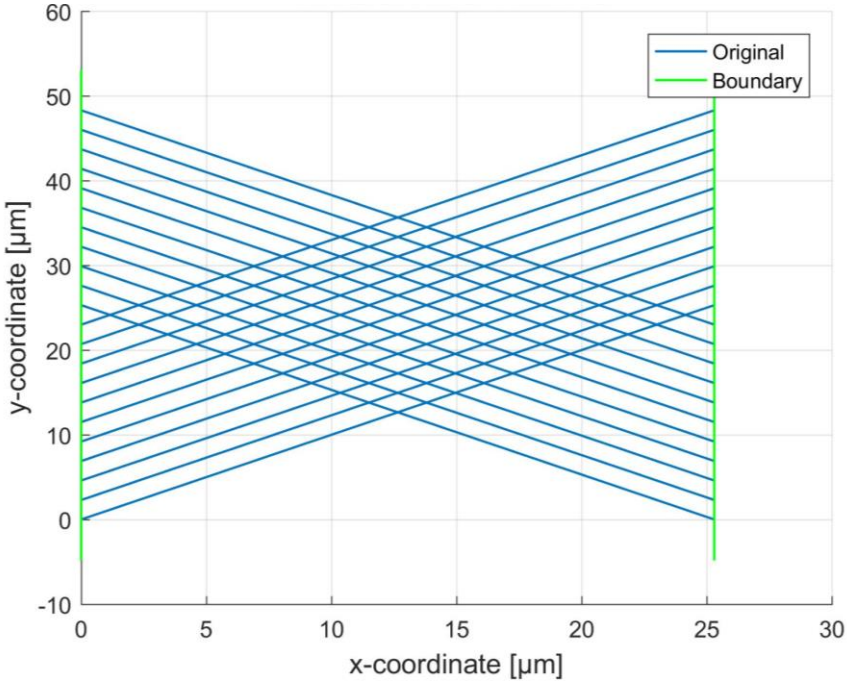

Figure 6. Final developed IM, with a distance between adjacent fibres equal to 2.3 µm, distance between boundaries equal to 25.3 µm, and fibre thickness of 1.05 µm. All fibres are orientated at ±45°, relative to the x-axis.

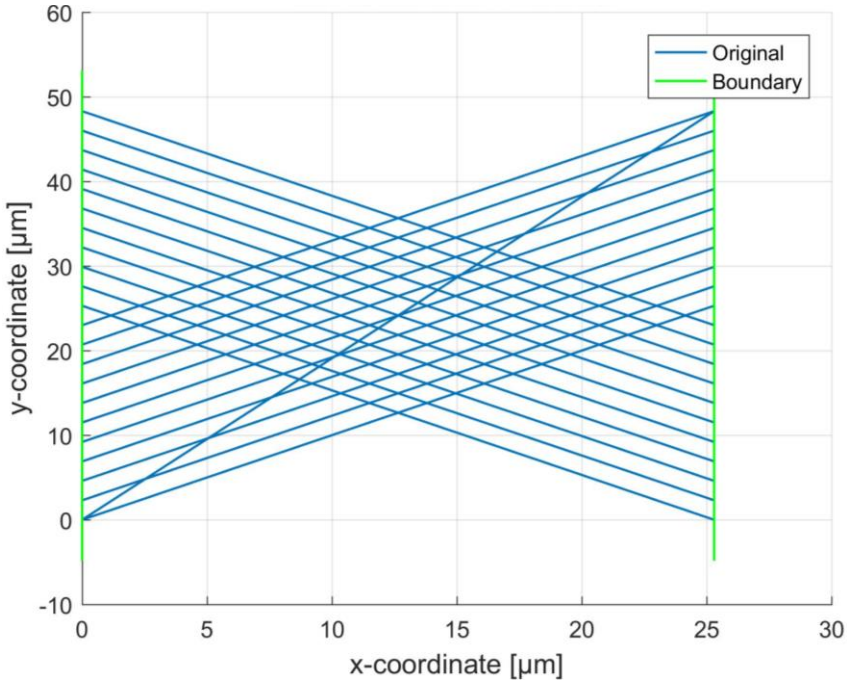

Figure 7. Final developed IMD, with a diagonal fibre attached to the bottom-left and top-right point. The distance between adjacent fibres equal 2.3 µm, distance between boundaries equal 25.3 µm, and the fibre thickness is 1.05 µm. All fibres are orientated at ±45°, relative to the x-axis, except for the diagonal fibre.

3.4 Specimen Model Development

During the initial stages of SM development, determining the geometry of the specimen was the first step, whereby the coordinates used in the model was determined from an image captured of a partially digested ILM sample (Tavakoli et al., 2017b) (Figure 8). The coordinates of the captured image could be determined due to the given scale bar, which was used to measure the two attachment points of each fibre, onto the lamellae. The fibres that were modelled were assumed to be in the upper region of the image, allowing for the development of a 2-dimensional model. However, for fibres that did have some depth, it was assumed that the depth component would have insignificant effect on the model, due to the small scale of the captured image. All fibres were assumed to be single fibres, without any branching, to simplify the model. The fibre thickness used in the SM, was equivalent to the fibre thickness used in the IM and IMD, therefore a fibre thickness of 1.05 µm was used in the SM. (Figure 9)

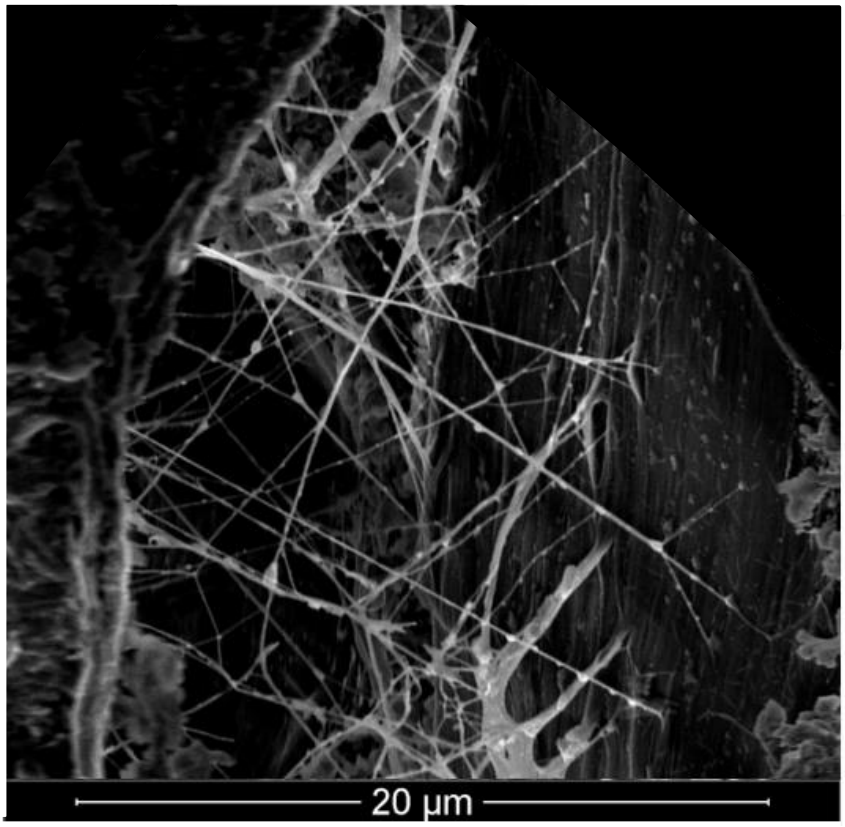

Figure 8. Image captured of the partially digested ovine specimen, revealing the ILM, which was used to develop the SM (Tavakoli et al., 2017b) (Appendix A shows what fibres were modelled in the SM, Figure 26).

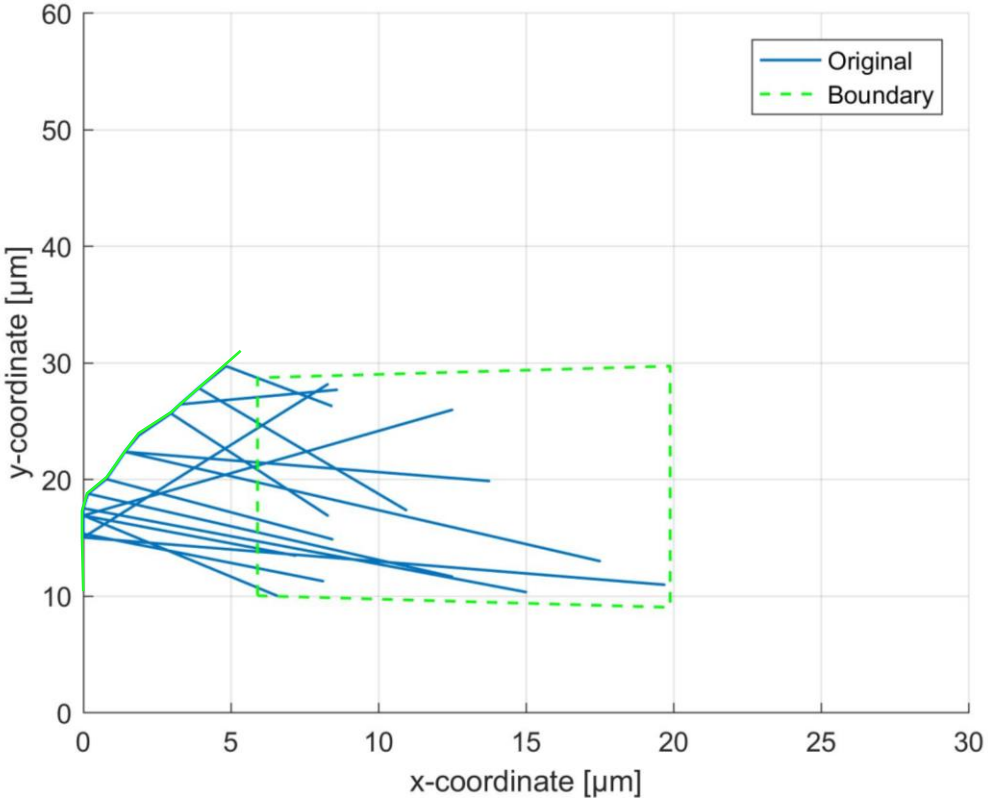

Figure 9. Final developed SM, with fibres orientated similarly to an image captured (Figure 8), where all fibres have a thickness of 1.05 µm (Appendix A). The right-hand boundary, indicated by the green dashed rectangle is for representative purposes and does not show the boundary to scale (Figure 9). A solid green line indicates the left-hand boundary.

3.5 Experimentation

Experimentation consisted of tensile and shear tests conducted on 1 mm × 10 mm ovine samples, with a maximum thickness of 50 µm (Tavakoli et al., 2017a). Two sample types were tested, intact and digested samples. Digested samples were attained by using a partial digestion technique (Tavakoli & Costi, 2016), during which the area surrounding the elastic fibres, within the ILM, were digested. Therefore, the experimental results of the digested samples were of great interest, since the developed models included elastic fibres without the surrounding matrix.

Each sample tested contained the ILM with adjacent lamellae and were fixed using superglue and sand paper (Figure 10) (Tavakoli et al., 2017a). Sample preparation was conducted through a microscope, after which the prepared sample was tested using a micro-tensile testing system (Cellscale, BioTester, Waterloo, Ontario, Canada). The

experiment was displacement controlled, during which 40% strain was applied to each sample at varying strain rates (1, 10, 100 Hz).

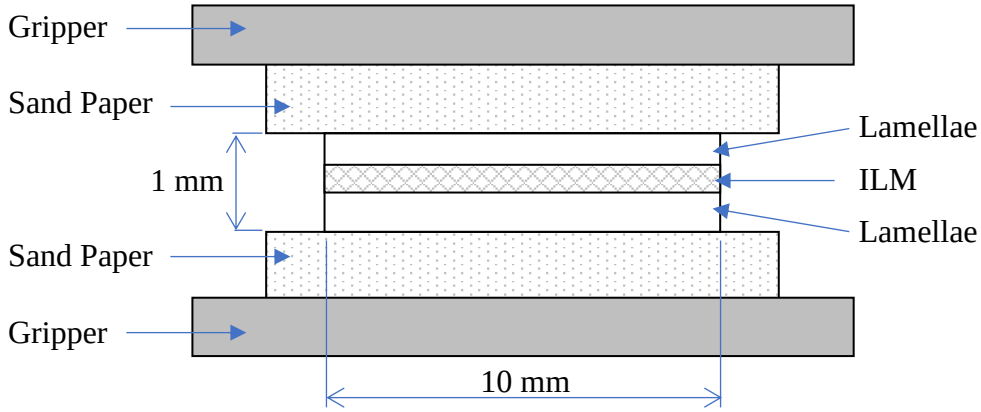

Figure 10. Schematic of the experimental setup, with a sample size of 1 mm × 10 mm. Grippers are on either side of the sample, with a combination of superglue and sandpaper to prevent the sample from slipping. The ILM is between two adjacent lamellae, which is placed in tension and shear at different strain rates of 1, 10, and 100 Hz (not to scale) (Tavakoli et al., 2017a). Refer to Figure 11 for a test image.

During experimentation, the final displacement of the ILM was approximately 116 µm (Figure 11). Therefore, in the IM and IMD the final stretched position of the model was 116 µm. The SM was significantly smaller than the IM and IMD, therefore an equivalent strain percentage was applied to the model, which was approximately 358.5% strain.

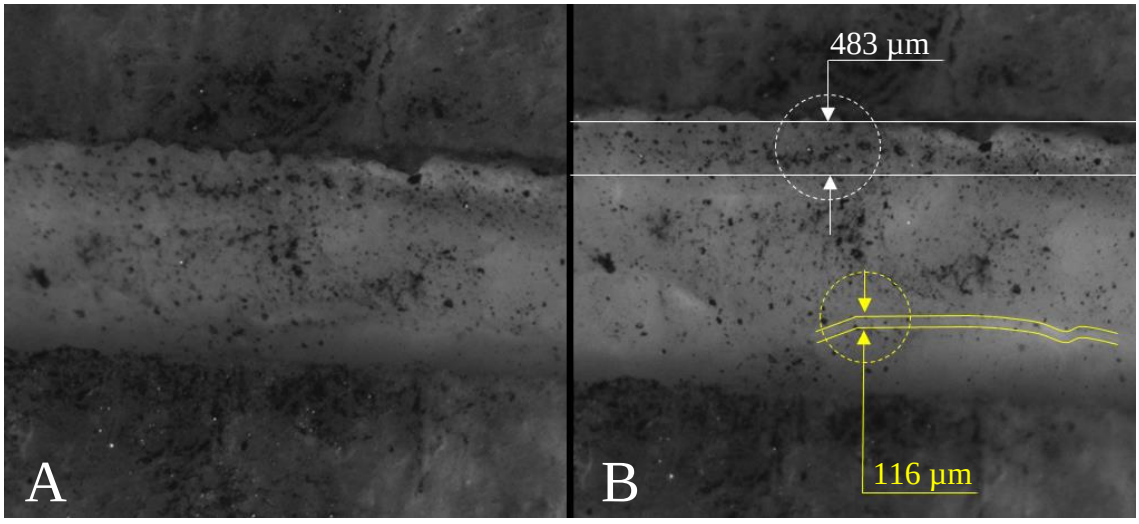

Figure 11. Experimental sample, placed under tension. (A) The unstretched sample, used as a reference. (B) The stretched sample displaced at 483 µm, shown in white. The ILM has a final stretched value of 116 µm, shown in yellow.

3.5.1 Applied Load per Fibre

The experimental applied load was measured during testing, which was used to validate the developed model, by calculating the equivalent load per fibre within the ILM (Table 1). Although the stress results were measured during testing, the stress results included both lamellae and the ILM, where the ILM had a significantly lower cross-sectional area than the lamellae in the digested samples. Therefore, it was determined that the stress within the ILM would not be equivalent to the measured experimental stress and using the applied load to validate the model would be more appropriate.

Table 1. The load per fibre was determined from an average experimental applied load and the total number of fibres within an area, per sample (Appendix A).

Average applied load [N]	Number of fibres per area [fibres/m^2]	Number of fibres in sample area [fibres/sample]	Average applied load, per fibre [N]
0.53	50,000,000,000	500,000	1.06E-06

3.5.2 Computational Young's Modulus

The linear modulus was determined from experimental results. However, due to the tested sample including both lamellae and ILM, it was determined that the linear modulus from the experimental results was not suitable to define the mechanical properties of the developed models, which represents the ILM in isolation. Therefore, the computational Young's Modulus of the elastic fibres, within the models, had to be determined by means of convergence.

Elastin in isolation has a Young's Modulus of 0.5 MPa (Smith & Fazzalari, 2009). Therefore, 0.5 MPa was used as a starting value at a strain rate of 1 Hz. The Young's Modulus used for the remaining strain rates, 10 Hz and 100 Hz, was determined from the ratio between the experimentally measured linear modulus, at varying strain rate (Table 2). The Young's Modulus values used, were a starting point for all the models, with the intention of altering the Young's Modulus until the computationally determined load converged to the experimentally applied load.

After simulating the IM, it was determined that the Young's Modulus used, at varying strain rate, output a computational applied load similar to the experimental applied load

(Table 5, Table 8 and Table 11). Therefore, the IM model was validated, and the Young's Modulus values used were appropriate (Table 2).

Table 2. Experimental results of the linear modulus, standard deviation (SD) of the experimental results (Tavakoli et al., 2017a), and computational Young's Modulus.

	Strain rate **[Hz]**	**Experimental linear modulus** **[kPa]**	**SD** **[±]**	**Difference between varying strain rate** [%]	**Computational Young's Modulus** **[MPa]**
Tension	**1**	0.7	0.51	0	0.50
	10	1.03	0.63	47.14	0.74
	100	1.35	0.57	31.07	0.96
Shear	**1**	0.63	0.5	0	0.50
	10	0.9	0.66	42.86	0.71
	100	1.27	0.86	41.11	1.01

3.6 Equations

Each model was developed in Matlab (The MathWorks, R2016a) to initially determine the load along each fibre, using FE methods and modelling the fibres as springs, from which the normal stress along the fibre was determined, σ (Figure 12).

3.6.1 Computational Applied Load

The fibres within each model were represented as spring elements, which was achieved by using local and global force-displacement relations. Therefore, each fibre was represented as an element, with two nodes. Ultimately, the equation used within the models reflected the linear spring equation, for each element (Ugural & Fenster, 2011).

Equation 1 – Linear spring equation, for each element

$$\{F\} = [K_{BC}]\{\delta\}$$

Where,

F – Applied load matrix [N]

K_{BC} – Global stiffness matrix, with applied boundary conditions [N/m]

δ – Displacement matrix, representing the final stretched value of the model [m]

The stiffness matrix $[k]$, was determined using the local stiffness matrix.

Equation 2 – Local 2-dimensional stiffness matrix, for each element

$$[k] = \frac{AE}{L}\begin{bmatrix} c^2 & cs & -c^2 & -cs \\ cs & s^2 & -cs & -s^2 \\ -c^2 & -cs & c^2 & cs \\ -cs & -s^2 & cs & s^2 \end{bmatrix}$$

Where,

k – Local stiffness matrix [N/m]

A – Cross-sectional area of the element [m^2]

E – Young's Modulus of the element [Pa]

L – Length of the element [m]

c – Denotes cosθ, where θ is the angle of the element relative to the x-axis [°]

s – Denotes sinθ

The assembly of the global stiffness matrix was achieved by summing the local stiffness matrices, of each element, with the corresponding matrix locations (Equation 2). The corresponding matrices represented any over-lapping nodes, which allowed a full representation of the system. The resulting global stiffness matrix was a square matrix, with the number of rows and columns equivalent to double the number of nodes within the model, which consisted of various zeros and the local stiffness matrices in their corresponding locations. When the global stiffness matrix was assembled, boundary conditions had to be applied to the matrix to determine the applied loads within the model.

The boundary conditions applied to all the models, were reflected in the global stiffness matrix by changing its rows and columns of the boundary elements to zero. The boundary elements, within the global stiffness matrix, that had matching rows and columns, were changed to number ones. The static boundary of each model was the lamellae on the left-hand side, which did not undergo any displacement. The displacement of the right-hand boundary was strain controlled in the x-direction, with an equivalent strain applied computationally and experimentally, to all three model types.

Therefore, the global stiffness matrix with applied boundary conditions and the final displacement of the model, was used to determine the applied force at each node within the model (Equation 1).

3.6.2 Normal Stress

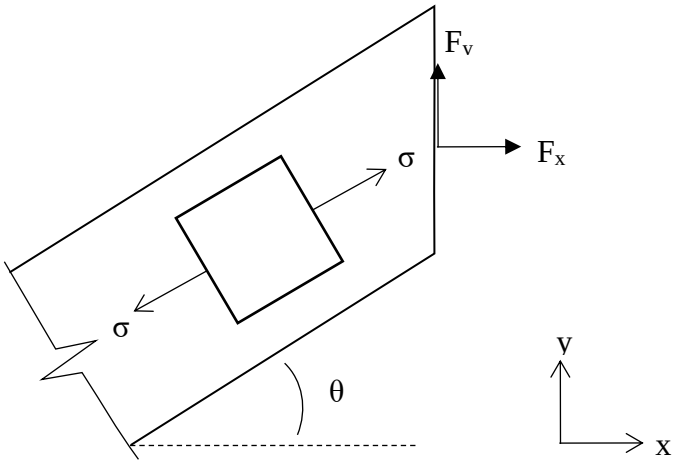

Figure 12. Schematic of the model output, which applies to all model types, with the x- and y-direction as shown. Enlarged cross-section of a fibre, orientated at angle θ, with applied loads F_x and F_y. The square in the fibre denotes an element within the model, which undergoes a normal stress σ, due to the applied load.

The resultant load was determined per fibre by using Pythagoras's theorem.

Equation 3 – Pythagoras's theorem, used to determine the resultant force per fibre

$$F = \sqrt{F_x^2 + F_y^2}$$

Using Hooke's Law and the resultant force, the stress along each fibre was determined.

Equation 4 – Hooke's Law, used to determine to stress along each fibre

$$\sigma = \frac{F}{A}$$

Where,

F – Resultant force [N]

F_x – Force in the x-direction [N]

F_y – Force in the y-direction [N]

σ – Normal stress, along the fibre [Pa]

Therefore, the force determined in Equation 1 was applied to Equation 4, from which the stress along each fibre was calculated, giving insight into the fibre contribution relative to the fibre orientation.

Chapter 4: Results

4.1 Ideal Model

The results obtained from the IM are consistent between fibres orientated at +45° and -45°, respectively, due to the symmetry of the model. Therefore, the results of each fibre orientation have been summarized and categorized into +45° and -45°, at varying strain rate. The angle and stress results relate to each fibre in the model.

4.1.1 Tension Loading

Table 3. IM computational results while undergoing tension, at varying strain rate. The results have been categorized into +45° and -45°, representing the two fibre orientations. All angles are relative to the x-axis.

Tension, results per fibre						
Strain Rate [Hz]	**Original Fibre Angle [°]**	**Final Fibre Angle [°]**	**Change in Angle [°]**	**Normal Strain ε [-]**	**Normal Stress σ [Pa]**	**Normal Stress σ [MPa]**
1	45.0	12.3	-32.7	2.32	896,245	0.90
	-45.0	-12.3	32.7	2.32	896,245	0.90
10	45.0	12.3	-32.7	2.32	1,326,443	1.33
	-45.0	-12.3	32.7	2.32	1,326,443	1.33
100	45.0	12.3	-32.7	2.32	1,720,791	1.72
	-45.0	-12.3	32.7	2.32	1,720,791	1.72

The computational results of the IM in tension have equivalent results in +45° and -45° orientated fibres, due to the symmetry of the model. The angle of every fibre decreased by 32.7°, caused by the elongation of the fibres in the x-direction. The strain is constant with varying strain rate, which is expected due to a constant strain being applied to each model. The normal stress within each fibre increases as the strain rate increases, caused by the viscoelastic properties of the ILM. (Table 3, Figure 13)

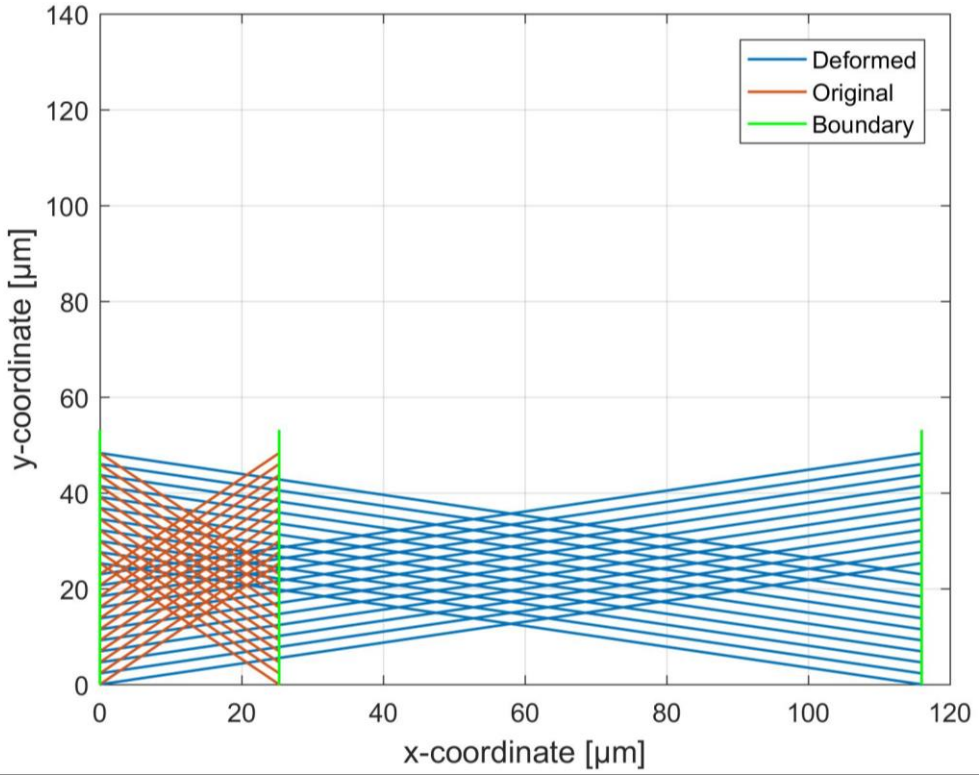

Figure 13. IM undergoing tension, with a final displacement of 116 µm or 358.5 % strain. The red line denotes fibres in the original position, at ±45°, the blue line denotes the fibres in the final stretched position, and the green line denotes the original and final boundary positions.

4.1.2 Shear Loading

Table 4. IM computational results while undergoing shear, at varying strain rate. The results have been categorized into +45° and -45°, representing the two fibre orientations. All angles are relative to the x-axis.

Shear, results per fibre						
Strain Rate [Hz]	**Original Fibre Angle [°]**	**Final Fibre Angle [°]**	**Change in Angle [°]**	**Normal Strain ε [-]**	**Normal Stress σ [Pa]**	**Normal Stress σ [MPa]**
1	45.0	77.7	32.7	2.32	896,245	0.90
	-45.0	68.9	113.9	0.96	896,245	0.90
10	45.0	77.7	32.7	2.32	1,272,668	1.27
	-45.0	68.9	113.9	0.96	1,272,668	1.27
100	45.0	77.7	32.7	2.32	1,810,415	1.81
	-45.0	68.9	113.9	0.96	1,810,415	1.81

The computational results of the IM in shear have varying results in +45° and -45° orientated fibres, due to the model undergoing shear. The angle of the +45° fibres

increased by 32.7° and the -45° fibres increased by 113.9°, caused by the elongation of the fibres in the y-direction. The strain varies in the +45° and -45° direction, which is expected due to the different changes in length depending on the direction of the fibres in the model. The normal stress within each fibre increases as the strain rate increased, caused by the viscoelastic properties of the ILM. (Table 4, Figure 14, Figure 15)

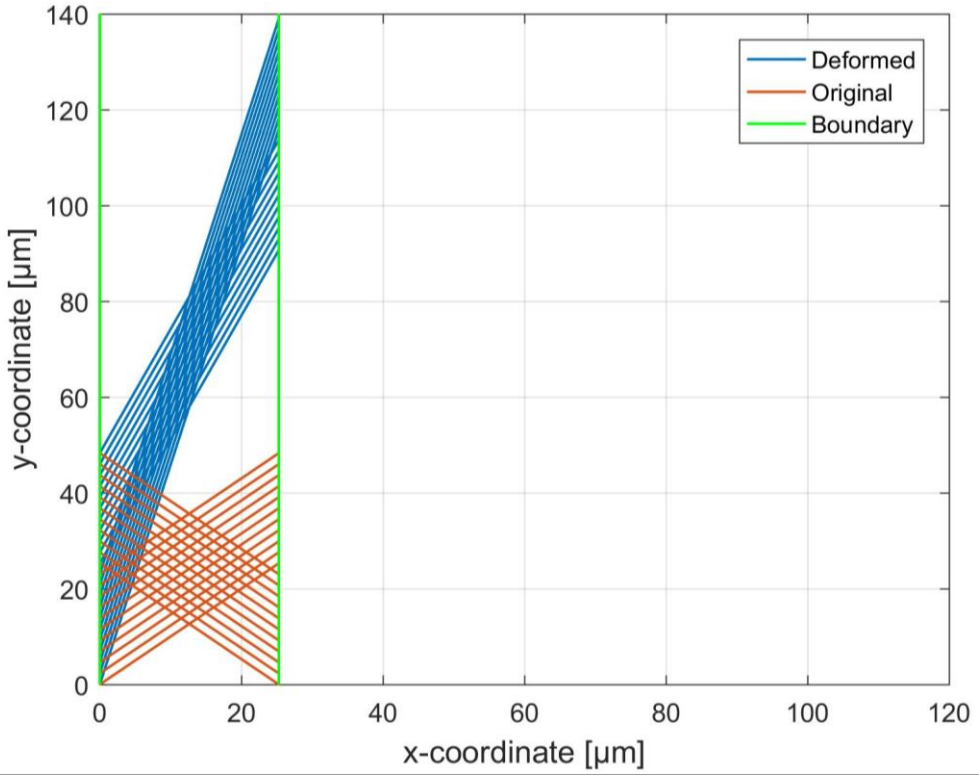

Figure 14. IM undergoing shear, with a final displacement of 116 µm or 358.5 % strain. The red line denotes fibres in the original position, at ±45°, the blue line denotes the fibres in the final stretched position, and the green line denotes the

original and final boundary positions. Refer to Figure 15 for an enlarged image, with the deformed fibres shown clearer.

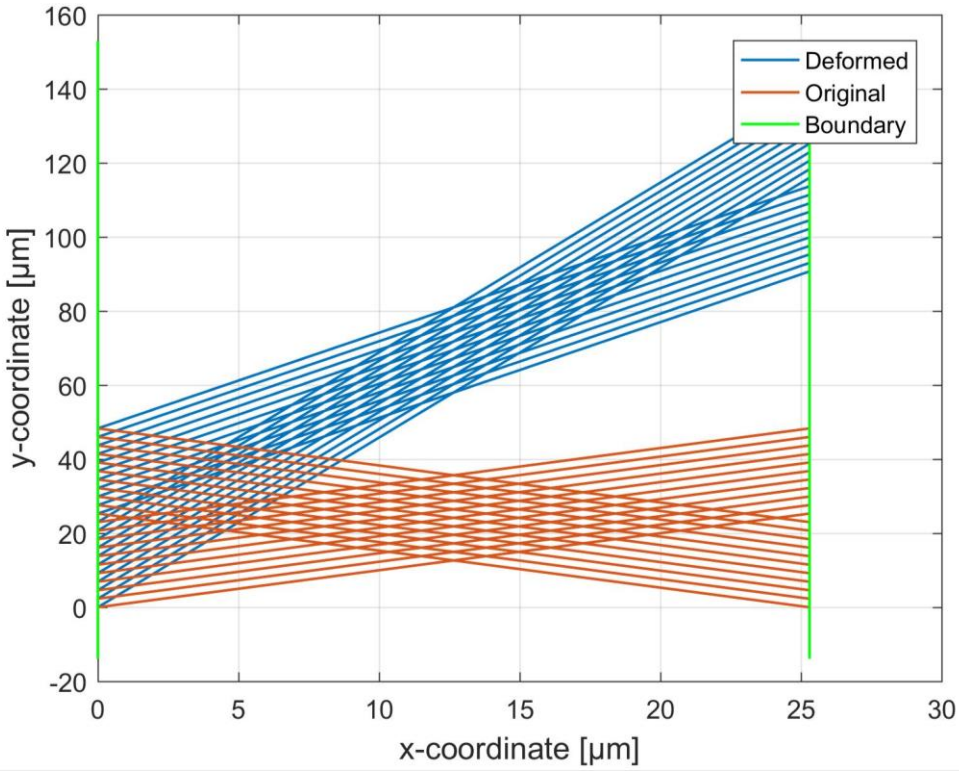

Figure 15. Enlarged image of Figure 14, with a different scalebar.

4.1.3 Computational Applied Load

Table 5. Computational applied load on the IM, in tension and shear, for 22 fibres. The applied load was summed in each direction, giving the equivalent load applied to the model, in the x- and y-direction. (Appendix B)

Strain Rate [Hz]	Direction	Tension	Shear	Experimental Applied Load, for 22 fibres [N]
		Applied Load [N]	Applied Load [N]	
1	**x**	1.21E-05	0	2.33E-05
	y	0	1.21E-05	
10	**x**	1.79E-05	0	
	y	0	1.71E-05	
100	**x**	2.32E-05	0	
	y	0	2.44E-05	

4.2 Ideal Model with Diagonal Fibre

The results obtained from the IMD are consistent between fibres orientated at +45° and -45°, respectively. Due to the diagonal fibre, three fibre angles exist in the original model. Therefore, the results of each fibre orientation have been summarized and categorized into +45°, -45°, and 62.4°, relative to the x-axis, at varying strain rate. The angle and normal stress results are of each fibre in the model.

4.2.1 Tension Loading

Table 6. IMD computational results while undergoing tension, at varying strain rate. The results have been categorized into +45°, +62.4° and -45°, representing the three fibre orientations. Two +45° categories exist, the first represents all but one fibre orientation, and the second represents the fibre attached to the same node as the diagonal fibre. All angles are relative to the x-axis.

Tension, results per fibre						
Strain Rate [Hz]	**Original Fibre Angle [°]**	**Final Fibre Angle [°]**	**Change in Angle [°]**	**Normal Strain ε [-]**	**Normal Stress σ [Pa]**	**Normal Stress σ [MPa]**
1	45.0	12.3	-32.7	2.32	896,245	0.90
	62.4	22.6	-39.7	1.30	385,797	0.39
	45.0	12.3	-32.7	2.32	896,379	0.90
	-45.0	-12.3	32.7	2.32	896,245	0.90
10	45.0	12.3	-32.7	2.32	1,326,443	1.33
	62.4	22.6	-39.7	1.30	570,979	0.57
	45.0	12.3	-32.7	2.32	1,326,641	1.33
	-45.0	-12.3	32.7	2.32	1,326,443	1.33
100	45.0	12.3	-32.7	2.32	1,720,791	1.72
	62.4	22.6	-39.7	1.30	740,730	0.74
	45.0	12.3	-32.7	2.32	1,721,047	1.72
	-45.0	-12.3	32.7	2.32	1,720,791	1.72

The computational results of the IMD in tension have equivalent results in ±45° orientated fibres, and different results in the diagonal fibre. The angle of the ±45° fibres decreased by 32.7°, equivalent to the IM, and the diagonal fibre decreased by 39.7°, from 62.4°, caused by the elongation of the fibres in the x-direction. The strain is relatively constant with varying strain rate for the ±45° fibres, similar to the IM. However, the strain within the diagonal fibre is less, which is caused by the diagonal fibre having a different change in length and normal stress, compared to the ±45° fibres. The normal stress within

each fibre increases as the strain rate increases, caused by the viscoelastic properties of the ILM. (Table 6, Figure 16)

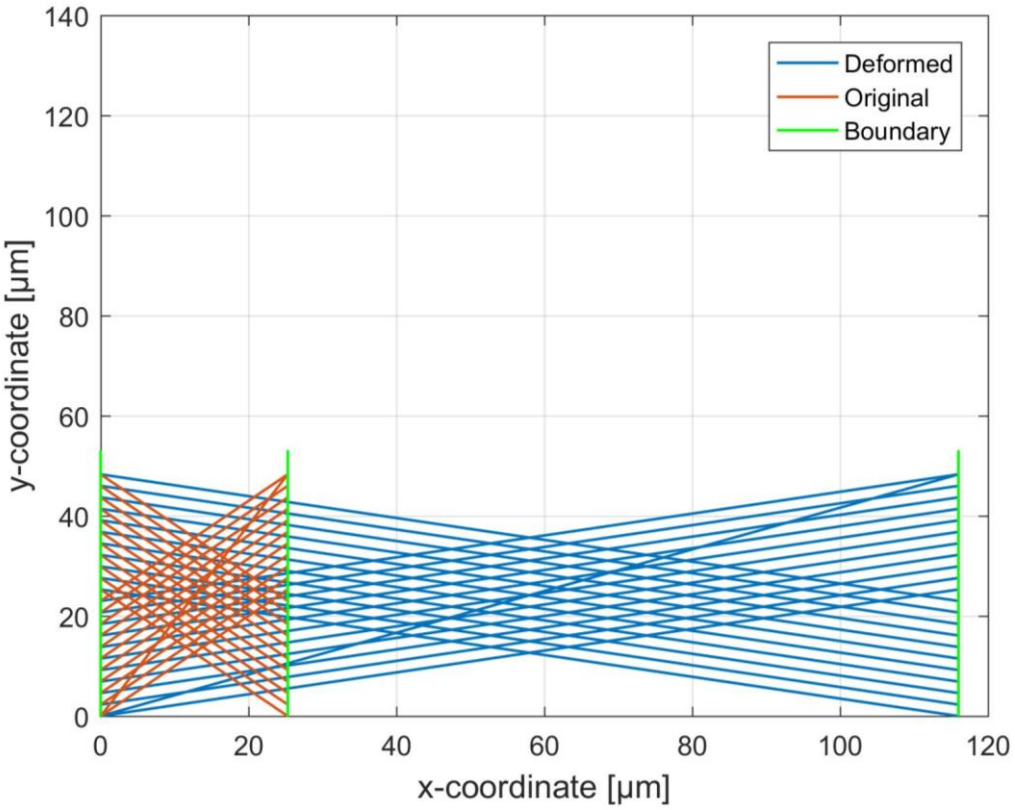

Figure 16. IMD undergoing tension, with a final displacement of 116 µm or 358.5 % strain. The red line denotes fibres in the original position, at ±45° and +62.4° relative to the x-axis, the blue line denotes the fibres in the final stretched position, and the green line denotes the original and final boundary positions.

4.2.2 Shear Loading

Table 7. IMD computational results while undergoing shear, at varying strain rate. The results have been categorized into +45°, +62.4° and -45°, representing the three fibre orientations. Two +45° categories exist, the first represents all but one fibre orientation, and the second represents the fibre attached to the same node as the diagonal fibre. All angles are relative to the x-axis.

Shear, results per fibre						
Strain Rate [Hz]	**Original Fibre Angle [°]**	**Final Fibre Angle [°]**	**Change in Angle [°]**	**Normal Strain ε [-]**	**Normal Stress σ [Pa]**	**Normal Stress σ [MPa]**
1	45.0	77.7	32.7	2.32	896,245	0.90
	62.4	79.7	17.3	1.59	736,521	0.74
	45.0	77.7	32.7	2.32	896,503	0.90
	-45.0	68.9	113.9	0.96	896,245	0.90
10	45.0	77.7	32.7	2.32	1,272,668	1.27
	62.4	79.7	17.3	1.59	1,045,860	1.05
	45.0	77.7	32.7	2.32	1,273,034	1.27
	-45.0	68.9	113.9	0.96	1,272,668	1.27
100	45.0	77.7	32.7	2.32	1,810,415	1.81
	62.4	79.7	17.3	1.59	1,487,772	1.49
	45.0	77.7	32.7	2.32	1,810,935	1.81
	-45.0	68.9	113.9	0.96	1,810,415	1.81

The computational results of the IMD in shear have varying results in ±45° orientated fibres, due to the model undergoing shear. The angle of the +45° fibres increase by 32.7° and the -45° fibres increase by 113.9°, equivalent to the IM in shear. The strain varies in the +45° and -45° direction, similar to that of the IM. However, the strain within the diagonal fibre is less, which is caused by the diagonal fibre having a different change in length and normal stress, compared to the ±45° fibres. The normal stress within each fibre increases as the strain rate increases, caused by the viscoelastic properties of the ILM. (Table 7, Figure 17)

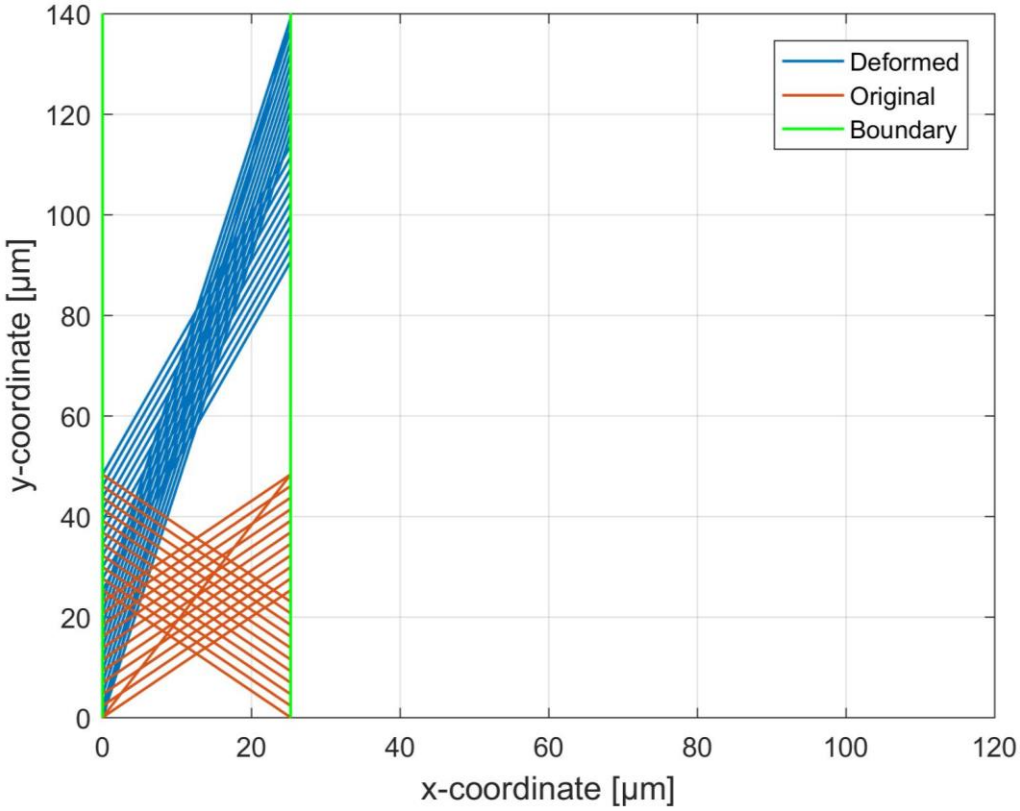

Figure 17. IMD undergoing shear, with a final displacement of 116 µm or 358.5 % strain. The red line denotes fibres in the original position, at ±45° and +62.4° relative to the x-axis, the blue line denotes the fibres in the final stretched position, and the green line denotes the original and final boundary positions. Refer to Figure 18 for an enlarged image, with the deformed fibres shown clearer.

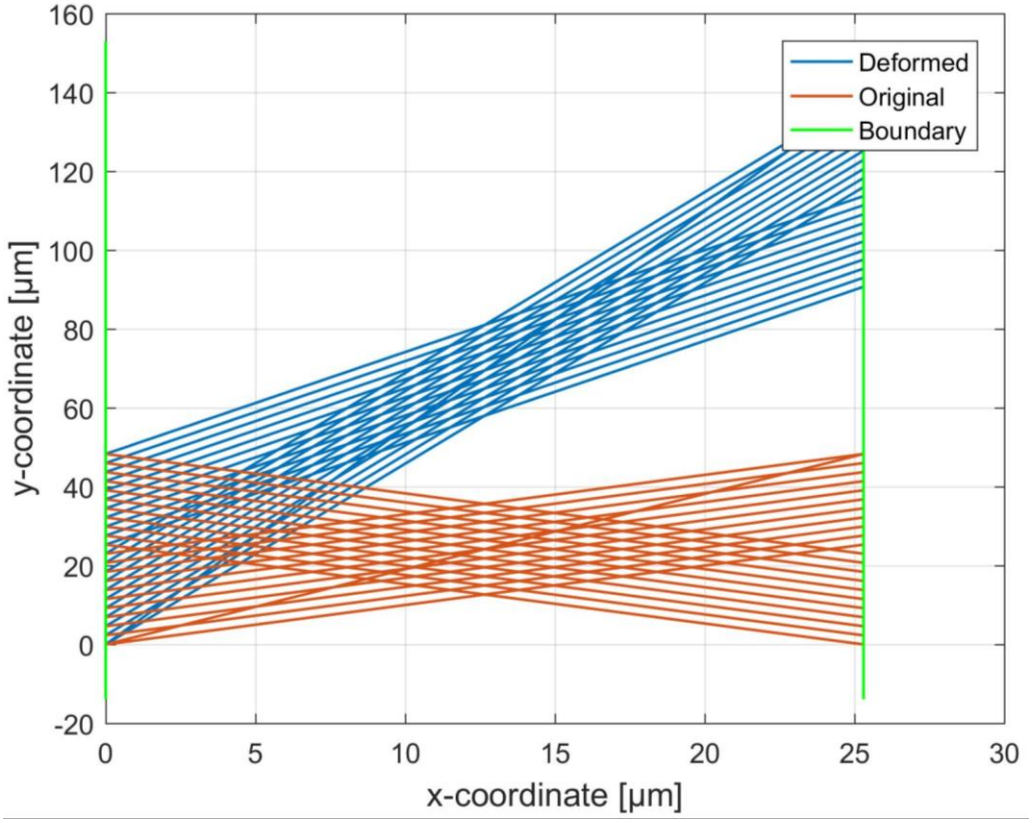

Figure 18. Enlarged image of Figure 17, with a different scalebar.

4.2.3 Computational Applied Load

Table 8. Computational applied load on the IMD, in tension and shear, for 23 fibres. The applied load was summed in each direction, giving the equivalent load applied to the model, in the x- and y-direction. (Appendix B)

Strain Rate [Hz]	Direction	Tension	Shear	Experimental Applied Load, for 23 fibres [N]
		Applied Load [N]	Applied Load [N]	
1	**x**	1.22E-05	0	2.44E-05
	y	0	1.26E-05	
10	**x**	1.81E-05	0	
	y	0	1.79E-05	
100	**x**	2.35E-05	0	
	y	0	2.55E-05	

4.3 Specimen Model

Each fibre orientation within the SM varied, therefore an average of the results from the positively and negatively orientated fibres was determined, respectively, at varying strain rates. The angle and normal stress results are within each fibre. (Appendix B)

4.3.1 Tension Loading

Table 9. SM computational results undergoing tension, at varying strain rate. The results are categorized into positive and negatively orientated fibres, from which an average was determined. All angles are relative to the x-axis. (Appendix B)

Tension, results per fibre						
Strain Rate [Hz]	**Original Fibre Angle [°]**	**Final Fibre Angle [°]**	**Change in Angle [°]**	**Normal Strain ε [-]**	**Normal Stress σ [Pa]**	**Normal Stress σ [MPa]**
1	35.6	12.4	-23.3	2.5	1,120,106	1.1
	-33.3	-9.8	23.6	2.3	952,386	1.0
10	35.6	12.4	-23.3	2.5	1,657,756	1.66
	-33.3	-9.8	23.6	2.3	1,409,532	1.41
100	35.6	12.4	-23.3	2.5	2,150,603	2.15
	-33.3	-9.8	23.6	2.3	1,828,582	1.83

The computational results of the SM in tension have varying outputs between the +35.6° and -33.3° orientated fibres. The angle of the 35.6° fibre decreased by 23.3°, and the angle of the -33.3° fibre increased by 23.6°, caused by the elongation of the fibres in the x-direction. The strain is equal with fibres at equivalent orientation, however it does vary between positive and negatively orientated fibres, caused by the fibres having different changes in length. The normal stress within each fibre increases as the strain rate increases, caused by the viscoelastic properties of the ILM. (Table 9, Figure **19**, Figure 20).

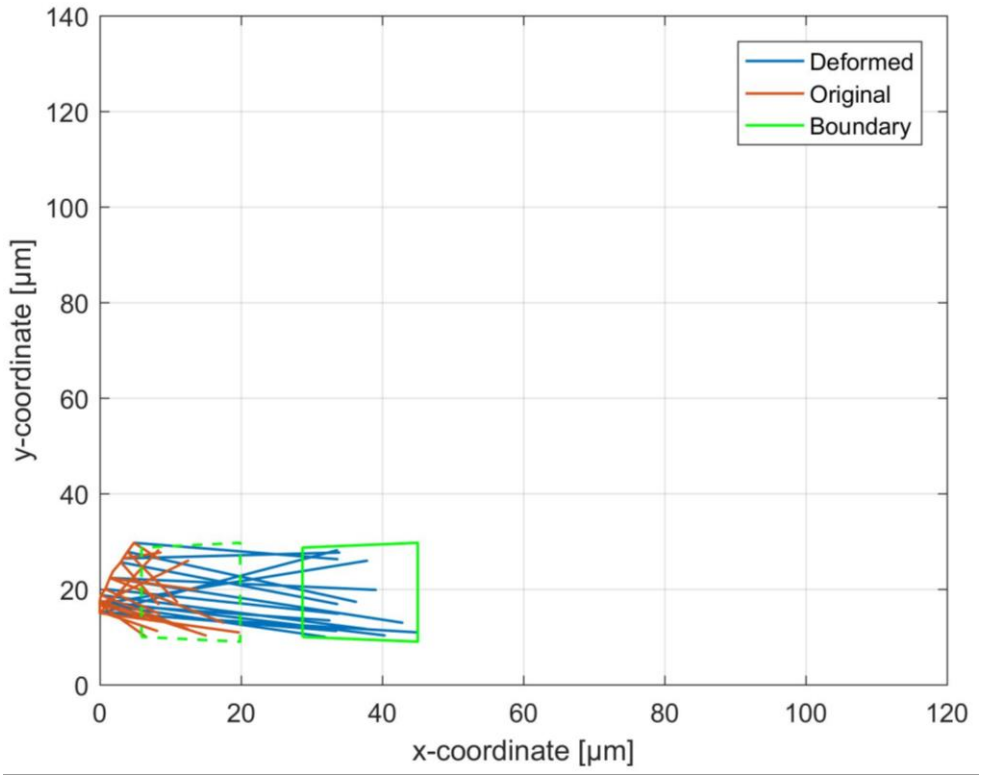

Figure 19**. SM undergoing tension, displaced at 358.5 % strain. The red line denotes fibres in the original position, the blue line denotes the fibres in the final stretched position, and the dashed and solid green line denotes the original and final boundary positions, respectively. An enlarged image is shown in Figure 20.**

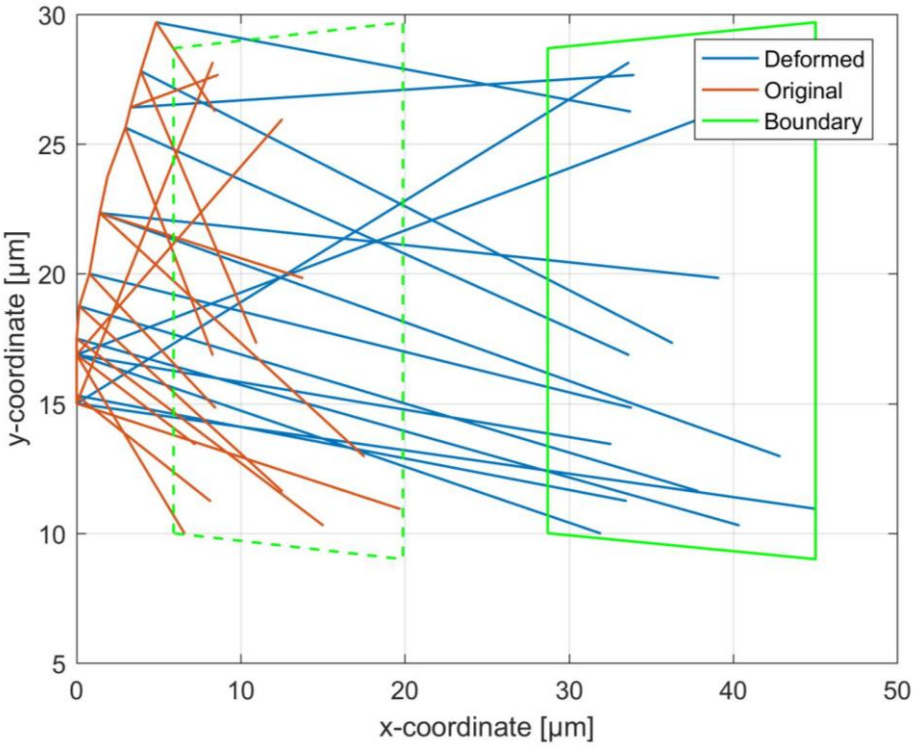

Figure 20. An enlarged image of Figure 19**, with a different scalebar.**

4.3.2 Shear Loading

Table 10. SM computational results undergoing shear, at varying strain rate. The results are categorized into positive and negatively orientated fibres, from which an average is determined. All angles are relative to the x-axis. (Appendix B)

Shear, results per fibre						
Strain Rate [Hz]	**Original Fibre Angle [°]**	**Final Fibre Angle [°]**	**Change in Angle [°]**	**Normal Strain ε [-]**	**Normal Stress σ [Pa]**	**Normal Stress σ [MPa]**
1	35.6	75.5	39.9	2.3	568,021	0.57
	-33.3	63.2	96.5	1.1	677,768	0.68
10	35.6	75.5	39.9	2.3	806,589	0.81
	-33.3	63.2	96.5	1.1	962,430	0.96
100	35.6	75.5	39.9	2.3	1,147,401	1.15
	-33.3	63.2	96.5	1.1	1,369,090	1.37

The computational results of the SM in shear have varying outputs between the +35.6° and -33.3° orientated fibres. The angle of the 35.6° fibre increased by 39.0°, and the angle of the -33.3° fibre increased by 96.5°, caused by the elongation of the fibres in the y-direction. The strain is relatively constant with fibres at equivalent orientation, however it does vary between positive and negatively orientated fibres, caused by the fibres having different changes in length and normal stress. The normal stress within each fibre increases as the strain rate increases, caused by the viscoelastic properties of the ILM. (Table 10, Figure 21, Figure 22)

4.3.3 Computational Applied Load

Table 11. Computational applied load on the SM, in tension and shear, for 15 fibres. The applied load was summed in each direction, giving the equivalent load applied to the model, in the x- and y-direction. (Appendix B)

Strain Rate [Hz]	**Direction**	**Tension**	**Shear**	**Experimental Applied Load, for 15 fibres [N]**
		Applied Load [N]	**Applied Load [N]**	
1	**x**	1.06E-05	0	1.59E-05
	y	0	5.28E-06	
10	**x**	1.58E-05	0	
	y	0	7.50E-06	
100	**x**	2.04E-05	0	
	y	0	1.07E-05	

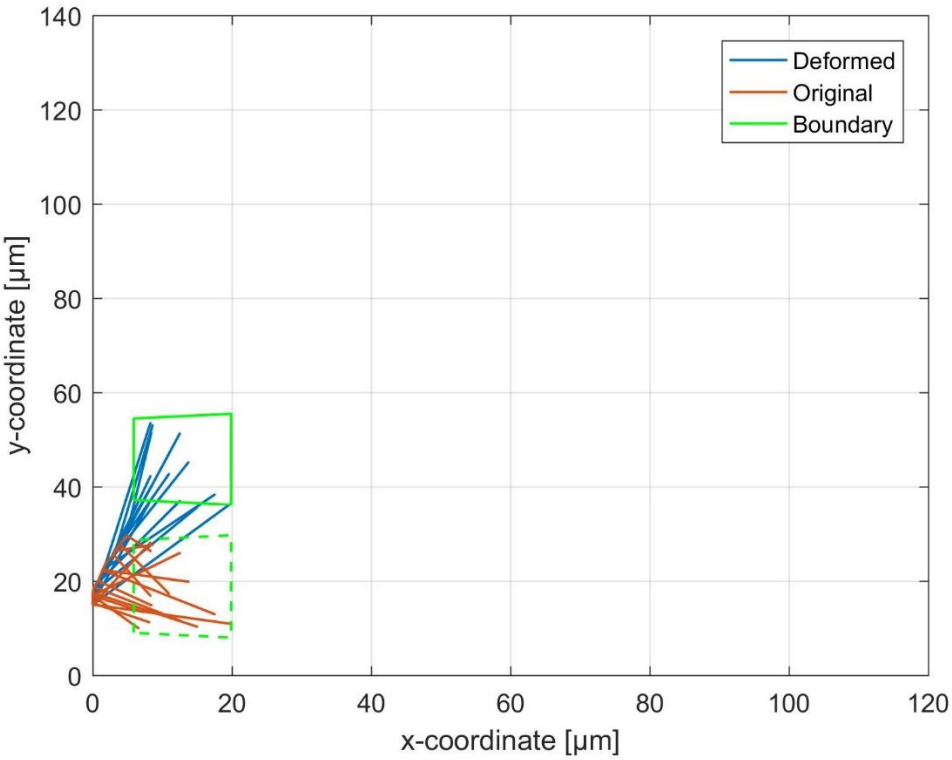

Figure 21. SM undergoing shear, displaced at 358.5 % strain. The red line denotes fibres in the original position, the blue line denotes the fibres in the final stretched position, and the dashed and solid green line denotes the original and final boundary positions, respectively. An enlarged image is shown in Figure 22.

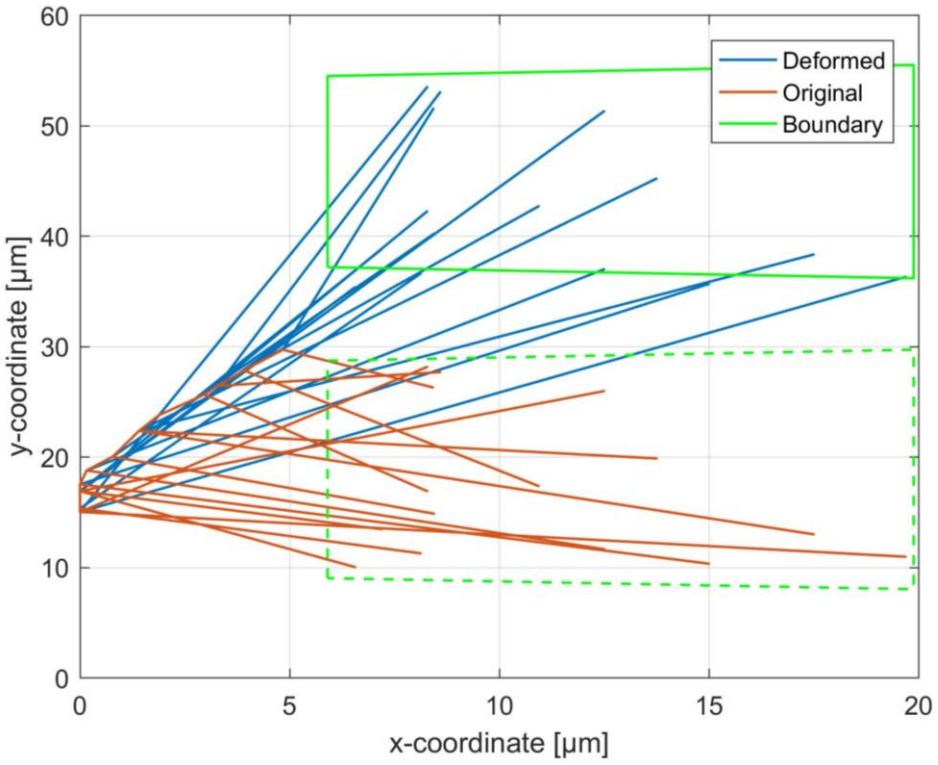

Figure 22. An enlarged image of Figure 21, with a different scalebar.

Chapter 5: Discussion

This study aimed to develop and validate a micro-finite element model of the ILM, and gain an understanding of how the fibre orientation within the ILM contributes to the mechanics of the system. Three model types exist: the IM, IMD and SM. The IM acted as a reference for the IMD and SM, as the IM was a symmetrical and simplified model. The IM was validated by comparing its computational applied load results with the experimentally measured applied load. When the IM was validated, equivalent parameters used in the IM, such as the geometry and Young's Modulus, were applied to the IMD and SM. Therefore, the effect of any variation between models was clear, from which an understanding was gained of how the fibre orientation contributed to the system.

The main limitation in this study concerns the method used to model the ILM fibres, whereby the fibres were not able to displace perpendicular to itself due to representing the fibres as springs – and would ultimately cause the fibres to collapse. However, the applied strain exceeded 100%, therefore the length of each fibre increased during tension and shear preventing any fibre from collapsing. Another limitation was modelling in 2-dimensions, which prevented full representation of the ILM and simplified any in-plane stresses and strains that may be taking place. Therefore, any stresses or strains that do not take place along the x- or y-direction will not be measured in the developed models. It is believed that if the in-plane stresses and strains were considered that it could potentially cause some warping of the model and lamellae surface. Any warping of the model could potentially lead to either reduced or increased stresses and strains within the elastic fibres. Consequently, further study is required and the development of 3-dimensional models of the ILM could give insight into the in-plane stresses and strains, which could aid in the understanding of how the in-plane components influence the ILM. However, at the current stage, 3-dimensional images of the ILM have not been collected and could potentially be an area for further study. It was assumed that the depth component of the fibre orientation is insignificant, when compared to its length, and was therefore omitted allowing for 2-dimensional modelling. The main model that would be affected by the absence of the depth component is the SM. However, fibres that appeared to be in the upper region of the image and did not seem to span too far into the depth were modelled, allowing for the assumption that the model is approximately 2-dimensional. Therefore, it

was assumed that the depth component would have an insignificant effect on the model output.

5.1 Ideal Model

The main purpose of the IM was to initially validate the model, by comparing its output with experimental results. After validation, the modelling parameters used in the IM, such as the geometry and Young's Modulus, were applied to the IMD and SM. It was also used as a reference for the IMD and SM output, to determine how variations in fibre orientations contribute to the mechanics of the ILM.

5.1.1 Model Validation

The experimentally measured applied load was used to validate the IM, by comparing it to the computationally determined applied load. The experimental load per fibre was 1.06E-06 N (Table 1), therefore scaling for 22 fibres the applied load is 2.33E-05 N (Table 5), which was used to validate the IM. The computational load varied with the change in strain rate, and ranged from 1.21E-05 N to 2.32E-05 N under tension, and 1.21E-05 N to 2.44E-05 N in shear (Table 5). At a higher strain rate, the computational load was higher, which was caused by an increase in the Young's Modulus due to the viscoelastic properties of the ILM. Comparing the computational and experimental loads, it was noted that at a strain rate of 1 Hz the computational load was about half of the experimental load. However, at a higher strain rate, the computational load was almost equivalent to the experimental load. The increasing difference between loads at varying strain rates, could be due to the significant difference that exists between the experimental loads for varying samples. The experimental load varies from 0.35 N to 0.89 N, which is a likely contributor to the difference when comparing the computational and experimental loads, at varying strain rates (Table 13). Therefore, the difference between the minimum and maximum experimentally applied loads is approximately 40%. Consequently, the variation in the computational load, from the experimental, could be within the appropriate range. At 1 Hz strain rate the difference between the experimental and computational load is approximately 48%, exceeding the difference between the experimentally applied loads. At 10 Hz the maximum difference between the experimental and computational load is approximately 27%, and at 100 Hz the difference is below 5%. Therefore, at 10 Hz and 100 Hz the computational model could be considered validated, as the difference is within the experimental load difference of 40%.

5.1.2 Tension

The results of the IM in tension were similar in the +45° and -45° fibre orientations, with an equivalent magnitude and opposing sign (Table 3, Figure 13). The equivalent results in fibre orientation was expected, due to the symmetry of the IM. The normal stress increased as the strain rate increased, due to the variation in Young's Modulus caused by the viscoelastic properties of the ILM. Therefore, the ±45° orientated fibres caused the stress distribution within the system to be even, which prevented any peak stresses within the system. Even stress distribution could be the reason the fibres are orientated at ±45° within the ILM (Tavakoli et al., 2017b), and to support loading in multi-directions.

5.1.3 Shear

In shear, the final fibre angle of the IM varied at the +45° and -45° fibre orientations (Table 4, Figure 14, Figure 15). The normal stress increased as the strain rate increased, similar to that in tension. The normal stress is equivalent in both +45° and -45° orientations, which is unexpected, due to the -45° changing in length less than the +45° fibre, as the model undergoes shear. The fibre at -45° was expected to have a lower normal stress than the +45° fibre. However, the way that the model has been developed, was to determine the applied load during the initial stage of load application – analysing the model at a static state. Therefore, the stresses were determined at the initial geometry, which would output the stresses the system undergoes when the load is applied – although, the -45° fibres would collapse during the initial displacement stage. Therefore, during the beginning stages of displacement application, the +45° fibres would tension and fully support the load, while the -45° fibres are collapsed. As the applied displacement increases, the -45° fibres would eventually start to tension, which would reduce the stress in the +45° fibres. Consequently, leading to the +45° having a higher normal stress.

In shear, the model output was as expected with the shear higher in the +45° fibres than the -45° fibres and was therefore used as a reference, to gain an understanding of how fibre orientation would contribute to the ILM mechanics – keeping in mind that the negatively orientated fibre stress would be reduced. Therefore, in stress, the limitation of the modelling method became evident and different modelling methods need to be explored further. It could be useful to develop a model that has a time dependent applied load, whereby the load would not be applied as a step input. Therefore, allowing the

tracking of fibre orientation and contribution over time. The computational applied load determined from the IM, could be used as a starting point for further model development.

5.2 Ideal Model with the Diagonal Fibre

The IMD was developed to gain an understanding of how a fibre orientated of more than 45°, relative to the x-axis, would contribute to the mechanics of the ILM. The results of the IMD were compared to the IM, the reference model. The normal stress results within each fibre increased as the strain rate increased, as seen in the IM, caused by the viscoelastic properties of the ILM.

5.2.1 Tension

The IMD in tension, output equivalent results in the +45° and -45° fibres, similar to that in the IM. However, the +45° fibre that was attached to the same node as the diagonal fibre (node number 22), had a slightly higher normal stress (Table 6, Figure 16). It was expected that the diagonal fibre would reduce the stress within the fibre sharing its node, as there is more support within the area. However, the increase in normal stress was a result of an increase in required applied load to achieve the desired displacement (Table 20), due to an increase in rigidity in the area – caused by the contribution of the diagonal fibre. Therefore, the diagonal fibre increased the support of the system, by resisting the applied displacement more than the fibres with separate nodes. The diagonal fibre had a lower normal stress than the ±45° fibres, which was expected, as the diagonal fibre was orientated more than +45°. However, it does indicate that an increase in the number of fibres attached to an area of the lamellae increases the stress within the ILM, under tension. Consequently, further study is required to better understand the complexity and stress distribution of the fibre attachment to the lamellae, as this study idealises the adhesion between the elastic fibres and lamellae boundary.

An increase in stress within the ILM is believed to contribute to the initial failure of the elastic fibres, leading to ultimate failure and delamination of lamellae, causing herniation (Smith et al., 2008). Therefore, high concentration of elastic fibres attaching to lamellae could be a potential cause and site for initial failure, such as fibre pull-out – leading to failure propagation and final failure. This result supports that fibre pull-out takes place during longitudinal tension (Iatridis & ap Gwynn, 2004), where peak stresses caused by high fibre concentration are a possible cause for failure.

5.2.2 Shear

Under shear, the IMD had equivalent results to the IM, similarly to that in tension (Table 7, Figure 17, Figure 18). However, it was expected that the -45° fibre would have a lower normal stress than the +45° fibre. The similarity between normal stresses at ±45° fibre orientations, is a result of the method used to develop the model – also noted in the IM results. The normal stress in the diagonal fibre is significantly higher under shear than in tension, which is relatively close to the +45° fibre results. An increased normal stress indicates that the diagonal fibre is better suited to support a shear loading direction, emphasising that a fibre with a larger orientation, relative to the x-axis, supports shear loading within the ILM. The normal stress within the +45° fibre, that shares the node of the diagonal fibre, is higher than the +45° fibres within the IM. The increase in normal stress indicates that the diagonal fibre, in conjunction with the +45° fibre, increases the required applied load for the system to reach the desired displacement. Therefore, the diagonal fibre increases the resistance within the ILM, preventing adjacent lamellae sliding relative to one another, which is the main form of deformation within the ILM (Michalek et al., 2009). It also indicates that high levels of stress induced by shear, likely caused by an increase in the concentration of fibre attachment points, could be a possible cause and contributor to failure propagation (Goel et al., 1995; Iatridis & ap Gwynn, 2004).

5.2.3 Computational Load

Within the IMD the computational load under tension ranged from 1.22E-05 N to 2.35E-05 N, for 1 Hz to 100 Hz strain rate, respectively. The computational applied load in shear ranged from 1.26E-05 N to 2.55E-05 N, for 1 Hz to 100 Hz strain rate, respectively. The experimental load for 23 fibres, within the IMD, was 2.44E-05 N (Table 8). The computational and experimental applied loads were approximately the same at 10 Hz and 100 Hz, where the biggest difference exist at 1 Hz strain rate with a computational load of almost half of the experimental load. Similarly, to the IM, it was assumed that due to the wide range of experimental loads, that a computational load that is half of the experimental load could be considered suitable. The applied load within the IMD is slightly higher than that for the IM, to achieve the desired displacement. The increase in computational load was caused by the diagonal fibre, that increased the rigidity of the system. In tension, the computational load was lower than in shear, which emphasises

that the diagonal fibre is more supportive in shear, leading to a higher applied load required to achieve the desired displacement. Therefore, indicating that high levels of stress induced by shear, is likely the primary cause of failure within the ILM (Gregory et al., 2011).

5.3 Specimen Model

The SM was developed to gain an understanding of how fibres orientated similarly to a specimen sample, contributes to the mechanics of the ILM. Similarly, the results of the SM were compared to the IM, the reference model, and reinforced if the ILM could be idealised. The normal stress results within each fibre increased as the strain rate increased, as seen in the IM, which was caused by the viscoelastic properties of the ILM. The results of the SM were categorized into positive and negatively orientated fibres, relative to the x-axis. The categorised values were then averaged, which was compared to the IM results, to determine how the specimen fibre orientations contribute to the mechanics of the ILM (Table 9, Table 10).

The averaged results of the positive and negative fibre orientations, of the SM, were almost similar in magnitude, between the 35.6° and -33.3° results, with a lesser difference at 1 Hz and greater difference at 100 Hz strain rate. Although, it was expected that the average fibre orientation would be closer to ±45°, instead there was approximately ±10° difference between the IM and SM fibre orientations. A significant percentage of the fibres were negatively orientated, therefore not fully representing different fibre orientations (Figure 26). If a larger specimen size was modelled, it would have included more fibre orientations and may have averaged to a magnitude closer to ±45°, therefore further development of the SM model could be meaningful.

5.3.1 Tension

In tension, the SM normal stress results were greater than that in the IM (Table 9, Figure **19**, Figure 20). The difference was caused by the complexity of the SM, whereby each fibre had a different length and orientation, leading to great variations in the determined normal stress (Table 16). However, the SM normal stress results are in a somewhat similar range to that of the IM, where the SM ranged from 1.1 MPa to 2.15 MPa, and the IM ranged from 0.9 MPa to 1.72 MPa. Therefore, the ILM could potentially be idealised,

which would aid the understanding of the inter-lamellar interactions. Although, further studies do need to be conducted to support the idealised model.

5.3.2 Shear

Under shear, the SM had lower normal stress results than that in tension, indicating that the SM fibre orientation was better adapted to shear loading (Table 10, Figure 21, Figure 22). However, it was expected that the normal stress in the negatively orientated fibres would have a lower stress, than the positively orientated fibres, which could have been caused by the method used to develop the model – which was also apparent in the IM. Comparing the SM normal stress to that of the IM, the SM had significantly lower stress results, emphasising that the SM may be better structured to support shear loading. The SM normal stress results were somewhat similar to the IMD stress results, which could indicate that the IMD is a better suited idealized model of the ILM. However, further study is required to support which model is better suited to represent an idealised structure of the ILM.

5.3.3 Computational Load

Within the SM, the computational load under tension ranged from 1.06E-05 N to 2.04E-05 N, for 1 Hz to 100 Hz strain rate, respectively. The computational applied load in shear, ranged from 5.28E-06 N to 1.07E-05 N, for 1 Hz to 100 Hz strain rate, respectively. The experimental load for 15 fibres, within the SM, was 1.59E-05 N (Table 11). The computational and experimental load are very similar in tension, where the computational load at 10 Hz, 1.58E-05, was almost identical. In shear, the computational load is about half of the experimental load, which might be caused by the reduced amount of fibres in the positive orientation. Therefore, a reduced amount of fibres exists within the SM that are adapted to support a shear loading regime. As a result, further study is required to better understand the mechanics of the SM, which could be achieved by modelling a larger specimen size and sample count.

5.4 Experimental and Computational Young's Modulus

The experimentally measured linear modulus ranged from 0.7 kPa to 1.35 kPa (unpublished) (Tavakoli et al., 2017a), whereas the Young's Modulus used in the models was greater by a magnitude of 10^3. The starting Young's Modulus was 0.5 MPa, which was a predetermined value for elastin in isolation (Smith & Fazzalari, 2009). The

significant difference between experimental and computational Young's Modulus could have been caused by the scale of the developed models, where numerous models would be required to represent an equivalent area of the tested sample. Therefore, the developed model represents a segment of fibres within the tested sample. Extending the model across an area equivalent to the tested sample – equal fibres in both experimental and computational model – would reduce the Young's Modulus of the combined model segments, or the entire system. However, each model was developed with the ILM in isolation, and the Young's Modulus applies to each fibre, not the entire system. Consequently, causing some differences between the experimental and computational mechanical properties. The experimental properties are of the entire tested sample and the computational properties reflect each fibre within the ILM, which is also in isolation.

Another cause of variation, was the structures present within the tested sample. The experiment conducted consisted of testing both ILM and adjacent lamellae, therefore, the linear modulus determined did not represent the ILM separately, which was required for developing the models. Consequently, the experimentally measured stress and linear modulus included both ILM and adjacent lamellae, which could not be used to validate or develop a model of the ILM in isolation. However, the experimentally applied load was normalized, by determining the load applied per fibre, allowing the IM to be validated.

Chapter 6: Conclusion

Although numerous studies have been conducted on the AF, limited studies exist at the microscale, the scale at which the ILM is present. Therefore, there is a gap in knowledge surrounding the properties and functions of the ILM. This study developed and validated a model that represented the ILM, from which an understanding was gained of how the fibre orientation within the ILM contribute to the mechanics of the system.

Under tension, along the x-axis, it was determined that fibres orientated closer to the x-axis, better support the ILM due to an increase in the computational applied load. Therefore, the fibres orientated closer to the x-axis, better support tension directional loading, ultimately preventing adjacent lamellae from moving further from one another. During shear, along the y-axis, it was determined that as the fibre orientation increases, relative to the x-axis, that the required applied load also increases. Therefore, indicating that as fibres become more aligned with the direction of the lamellae, that better support exists in shear within the ILM, ultimately reducing adjacent lamellae sliding. Consequently, the fibre orientation within the ILM can support multidirectional loading, where peak stresses could be a potential cause of fibre failure, such as fibre pull-out.

It was determined that with an increase in fibre attachment points, in an area on the lamellae, increased the stress observed within the model, especially in shear. Therefore, an increase in fibre concentration within one area of the lamellae, could potentially be a cause of peak stresses within the ILM. Peak stresses could ultimately cause fibre failure, which is believed to be a probable cause of delamination and herniation. Consequently, shear loading is the primary cause of failure within the ILM.

In conclusion, this study acts as an initial stage, working towards developing a model that approximately represents the ILM. A model that correctly represents the ILM mechanics, would be highly beneficial in gaining a better understanding of the AF, and what possible loading directions and magnitude could cause fibre failure or herniation. It could also give great insight into tissue engineering, with the aim of developing a medical device of the IVD that closely replicates the physiological system. Although it is still unclear what exactly causes herniation within the AF, it is believed that fibre failure within the ILM could be a possible cause. Therefore, the development of a micro-finite element model of the ILM would give great insight into the mechanics of the AF.

Chapter 7: Future Work

This study was a starting point for the development of a micro-finite element model of the ILM. Therefore, various aspects of this study could be further explored and verified, by using a combination of experimentation and FE methods.

7.1 Experimentation

The 3-dimensional structure of the ILM is still unclear. Therefore, collecting images of the ILM, at different angles, could be a step towards better understanding its complex structure. However, due to the ILM becoming apparent in the microscale, obtaining images at different angles may be a challenge. Therefore, development of a repeatable technique to capture images at varying angles, to overcome this challenge, could be a potential area for further study. Furthermore, once a technique has been developed, it could be used to determine the complete architecture of the ILM, which could be used to develop a 3-dimensional model.

An alternative option, could be to push the bounds of MRI, with the goal of scanning structures at the microscale. The scanning could be done on a digested lamellae and ILM segment, which could then be used to reassemble the structure, revealing the ILM architecture. However, MRI is time consuming and prototyping would be very costly. Noise within the images could also become a major issue, especially at the microscale, leaving the images collected unusable or distorting the reconstructed images beyond repair. However, it could be a potential solution in the future.

7.2 Finite Element Methods

The FE method used in this study was to model the fibres within the ILM as springs, through the use of Matlab (The MathWorks, R2016a). However, in shear the model results had both higher and lower stresses within fibres than expected. It is believed that the model was representing a more rigid structure than intended, outputting unexpected stresses within fibres during shear loading. Therefore, using another FE method could better predict the outcome the ILM undergoing shear.

The ILM could potentially be modelled in Abaqus, however, with the current information it would be modelled 2-dimensionally, similarly to this study. It would be meaningful to apply a time dependant load, through which it would be possible to track fibre orientation

and gain an understanding of fibre contribution over time. The computational Young's Modulus, determined in this study, could be used as a starting value to describe the mechanical properties of the model, after which the computational applied load determined in this study could be used to validate the model.

Lastly, modelling a larger specimen area would give greater insight into fibre contribution relative to orientation, due to the specimen model including more fibres. Modelling three or more different specimen areas could also add to the understanding of the ILM architecture, from which an average between the models could be determined. Therefore, modelling a larger specimen area and a larger sample size, would add to the current knowledge of the function of the ILM, and validate if an idealised model does represent the mechanics of the ILM.

Appendix A : Methodology

A.1 Distance Between Adjacent Fibres

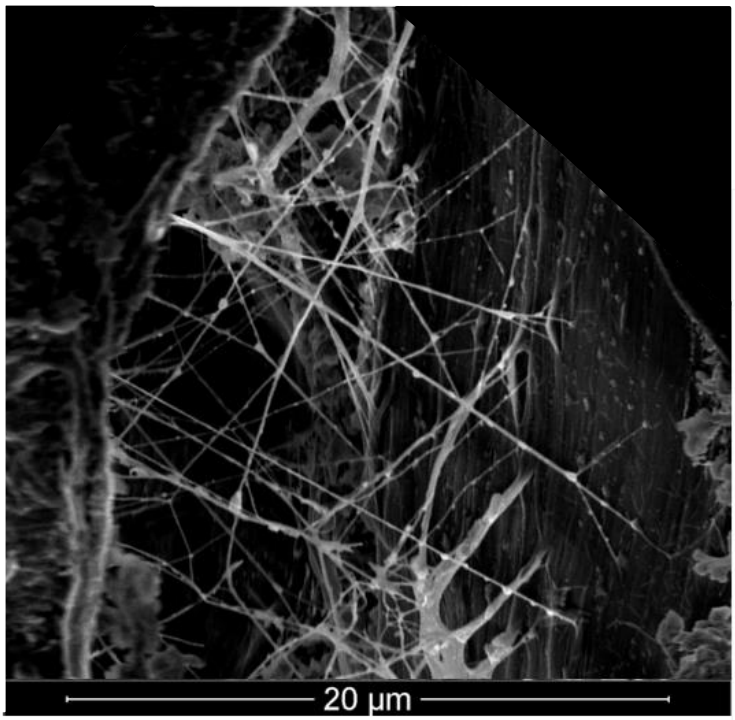

Figure 23. Image captured of the ILM, which was used to measure the distances between attachment points of adjacent fibres (Tavakoli et al., 2017b).

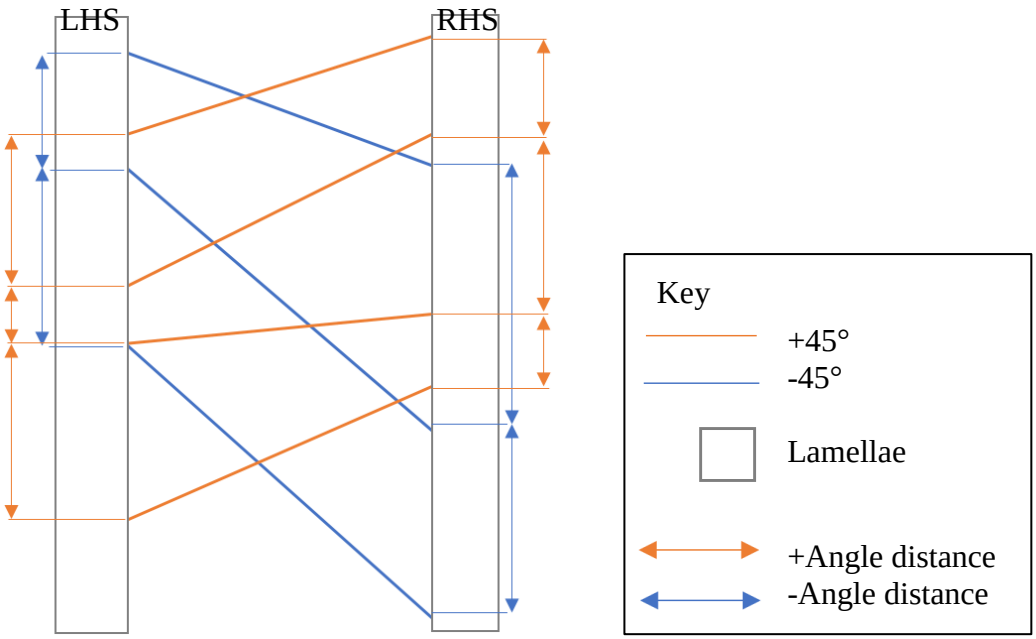

Figure 24. Schematic representing how the distances between adjacent fibres was measured, where the key shows the different elements within the schematic. LHS is the left-hand lamellae, and RHS is the right-hand lamellae.

Table 12. Distances measured between adjacent fibres, from an image captured of the ILM (Figure 23) (Tavakoli & Costi, 2016). The distance between adjacent fibres at a positive angle, +45°, and negative angle, -45°, were measured, respectively, and an average determined of 2.3 µm (Figure 24)

Angle [°]	LHS [µm]	RHS [µm]
+45	2.00 0.67 7.85	0.50 2.00 2.84 3.51
-45	1.84 0.67 2.51 2.34 3.67 1.50 1.84	0.33 1.00 2.00 0.50 1.50 1.67 0.84 2.51 8.85
Average of LHS and RHS [µm]	2.302	
SD of LHS and RHS [µm]	2.078	

A.2 Calculating Load per Fibre

The average applied load was determined by taking the average of 9 samples (Table 13)

Table 13. Applied load of 9 different samples from which an average is determined (unpublished) (Tavakoli et al., 2017a).

Sample number	Applied load [N]	Average applied load [N]	SD [N]
1	0.350	0.53	0.19
2	0.354		
3	0.420		
4	0.356		
5	0.510		
6	0.822		
7	0.893		
8	0.478		
9	0.603		

After determining the average load applied during experimentation, the number of fibres per area was calculated, to estimate how many fibres exist within a given area. Fibres were counted in images captured of the partially digested ILM, within a length of 20 µm, where the samples were approximately 30 µm thick (Figure 25) (Tavakoli & Costi, 2016).

Table 14. Number of fibres within a 20 µm height, in three images captured of partially digested ILM samples (Figure 25), with a sample thickness of 30 µm. Therefore, the total amount of fibres within a 20 µm × 30 µm area.

Image ID	Fibre count in 20 µm × 30 µm	Average fibre count in 20 µm × 30 µm, to the nearest fibre	Number of fibres per area [fibres/m^2]
A	26	30	50,000,000,000
B	28		
C	34		

To determine the load applied to each fibre, the amount of fibres within the tested sample was determined. Each sample was 1 mm × 10 mm, therefore the number of fibres was determined in each sample using the relationship shown in Table 14. Finally, from the total fibre count the force per fibre was determined (i.e. 0.53 N / 500,000 fibres) (Table 15).

Table 15. Number of fibres in the sample area, 1 mm × 10 mm.

Area in tested samples, 1 mm × 10 mm [m^2]	Number of fibres in sample area [fibres/sample]	Average applied load, per fibre [N]
0.00001	500,000	1.06E-06

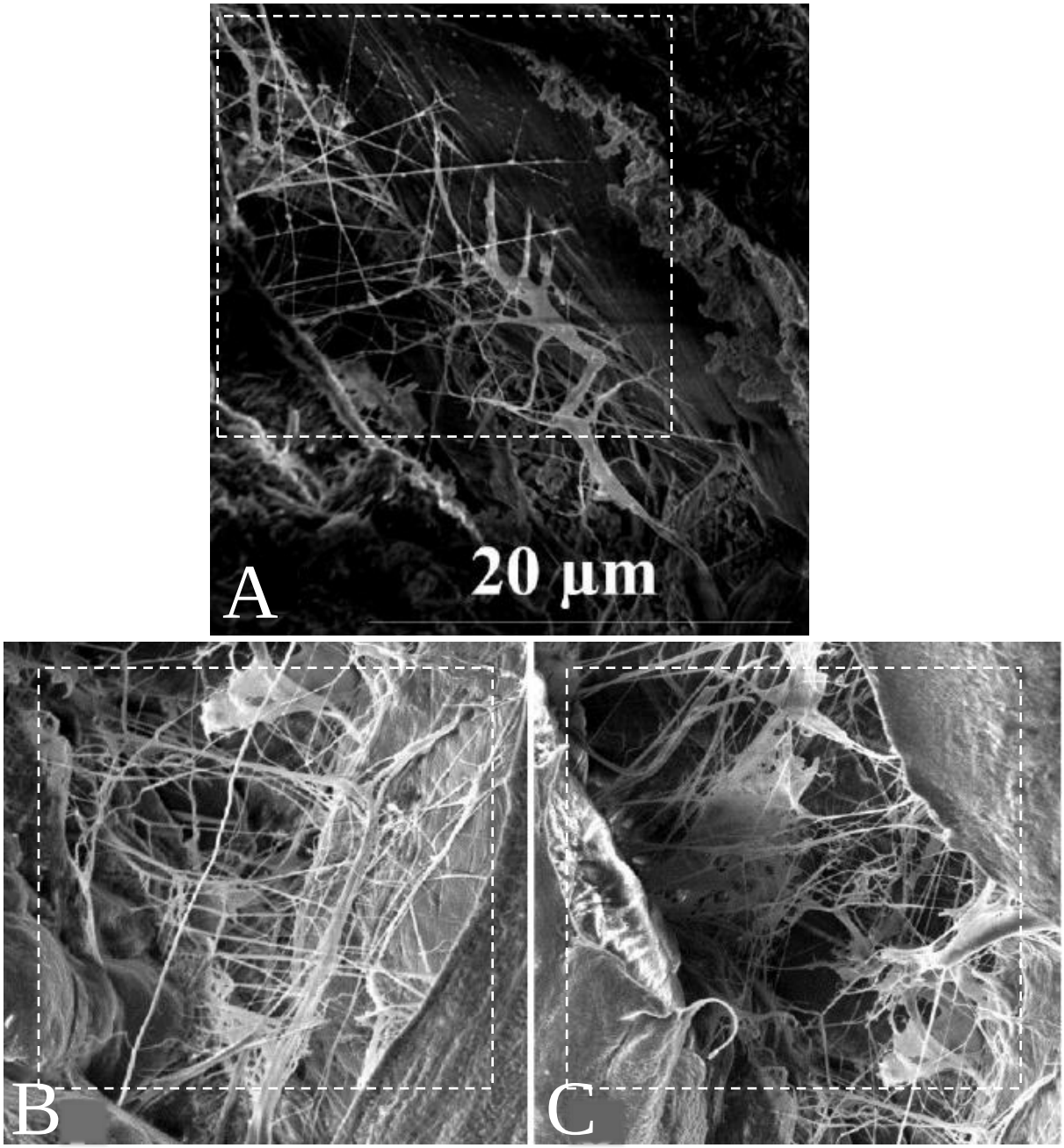

Figure 25. Images captured in three regions within the same ILM, A, B, and C. All samples had a thickness of 30 µm, from which fibres within a 20 µm height was counted. White dashed square indicates area in which fibres were counted (Tavakoli et al., 2017b).

A.3 Specimen Model Development

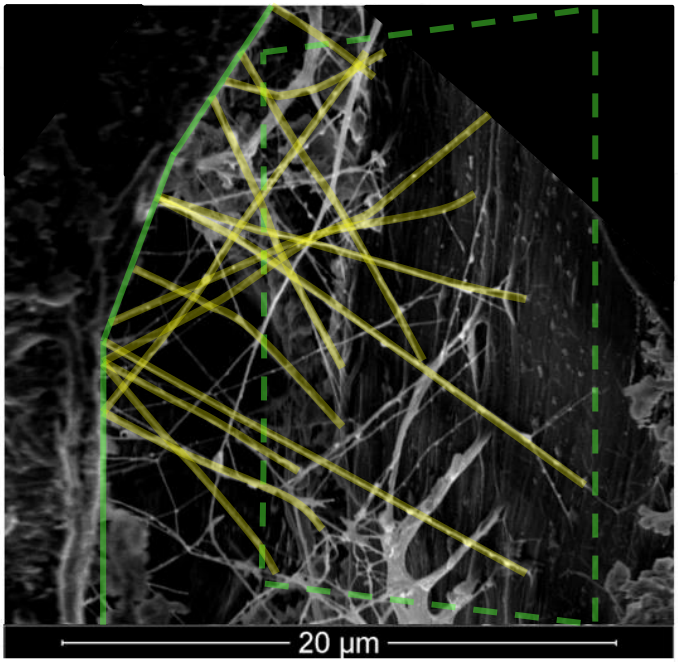

Figure 26. Image captured of the ILM, with a thickness of 30 µm, which was used to develop the SM (Tavakoli et al., 2017b). The fibres selected are highlighted in yellow, and were considered to be at the upper region of the sample thickness, to allow for modelling a 2-dimensional model. The fibres selected had a definite attachment point on the left-hand boundary, solid green line, and the end point of the fibre attached to the right-hand boundary, represented by the green dashed line.

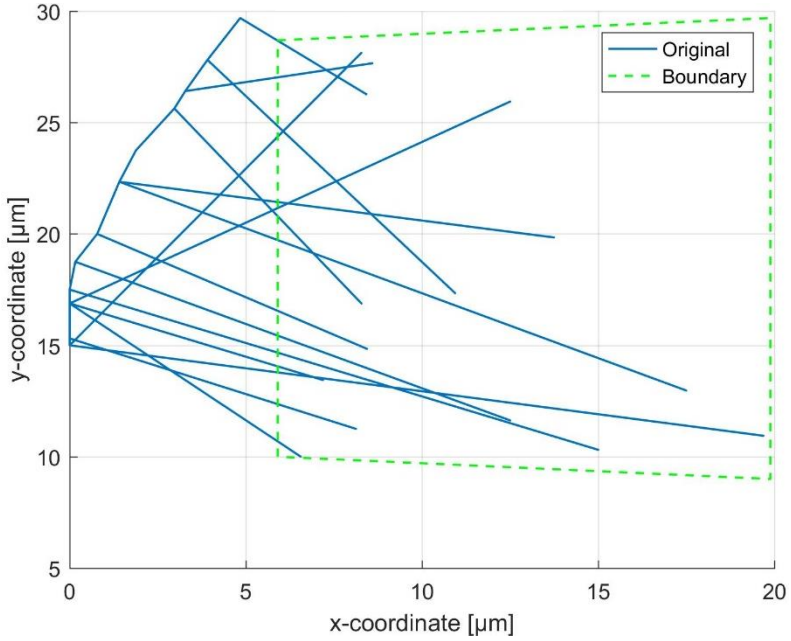

Figure 27. Final developed SM, a representation of the physiological system as shown in Figure 26.

Appendix B : Results

B.1 Specimen Model Computational Results

Table 16. SM computational results under tension, at varying strain rate. The varying strain rate is shown above separate tables, and the average of the results are shown below the data. The element number depicts the fibre count and was used as an ID number.

Tension – 1 Hz						
Element Number	**Original Fibre Angle [°]**	**Final Fibre Angle [°]**	**Change in angle [°]**	**Strain ε [-]**	**Normal Stress σ [Pa]**	**Normal Stress σ [MPa]**
1	57.8	21.3	36.4	1.3	435,336	0.44
2	-26.6	-6.9	19.6	2.7	1,247,682	1.25
3	-25.6	-10.1	15.5	1.5	686,782	0.69
4	-34.0	-8.9	25.1	2.6	1,137,638	1.14
5	-11.5	-3.8	7.7	2.0	986,157	0.99
6	-30.2	-12.7	17.5	1.3	587,965	0.59
7	13.2	2.3	10.9	4.6	2,260,542	2.26
8	-56.1	-17.9	38.2	1.7	559,983	0.56
9	-43.7	-6.8	36.9	4.9	1,839,473	1.84
10	-46.4	-12.2	34.2	2.4	919,644	0.92
11	-25.6	-6.0	19.5	3.1	1,433,780	1.43
12	35.9	13.5	22.5	1.5	664,439	0.66
13	-30.0	-10.7	19.3	1.7	770,218	0.77
14	-11.7	-5.2	6.5	1.2	617,166	0.62
15	-58.7	-15.9	42.8	2.1	642,148	0.64
Average^{+}	35.6	12.4	23.3	2.5	1,120,106	1.1
Average^{-}	-33.3	-9.8	23.6	2.3	952,386	1.0
10 Hz						
Element Number	**Original Fibre Angle [°]**	**Final Fibre Angle [°]**	**Change in angle [°]**	**Strain ε [-]**	**Normal Stress σ [Pa]**	**Normal Stress σ [MPa]**
1	57.8	21.3	36.4	1.3	644,297	0.64
2	-26.6	-6.9	19.6	2.7	1,846,570	1.85
3	-25.6	-10.1	15.5	1.5	1,016,437	1.02
4	-34.0	-8.9	25.1	2.6	1,683,704	1.68
5	-11.5	-3.8	7.7	2.0	1,459,513	1.46
6	-30.2	-12.7	17.5	1.3	870,188	0.87

7	13.2	2.3	10.9	4.6	3,345,602	3.35
8	-56.1	-17.9	38.2	1.7	828,774	0.83
9	-43.7	-6.8	36.9	4.9	2,722,420	2.72
10	-46.4	-12.2	34.2	2.4	1,361,073	1.36
11	-25.6	-6.0	19.5	3.1	2,121,995	2.12
12	35.9	13.5	22.5	1.5	983,370	0.98
13	-30.0	-10.7	19.3	1.7	1,139,923	1.14
14	-11.7	-5.2	6.5	1.2	913,405	0.91
15	-58.7	-15.9	42.8	2.1	950,379	0.95
Average^{+}	35.6	12.4	23.3	2.5	1,657,756	1.7
Average^{-}	-33.3	-9.8	23.6	2.3	1,409,532	1.4
100 Hz						
Element Number	**Original Fibre Angle [°]**	**Final Fibre Angle [°]**	**Change in angle [°]**	**Strain ε [-]**	**Normal Stress σ [Pa]**	**Normal Stress σ [MPa]**
1	57.8	21.3	36.4	1.3	835,845	0.84
2	-26.6	-6.9	19.6	2.7	2,395,550	2.40
3	-25.6	-10.1	15.5	1.5	1,318,621	1.32
4	-34.0	-8.9	25.1	2.6	2,184,265	2.18
5	-11.5	-3.8	7.7	2.0	1,893,422	1.89
6	-30.2	-12.7	17.5	1.3	1,128,893	1.13
7	13.2	2.3	10.9	4.6	4,340,240	4.34
8	-56.1	-17.9	38.2	1.7	1,075,167	1.08
9	-43.7	-6.8	36.9	4.9	3,531,788	3.53
10	-46.4	-12.2	34.2	2.4	1,765,716	1.77
11	-25.6	-6.0	19.5	3.1	2,752,858	2.75
12	35.9	13.5	22.5	1.5	1,275,723	1.28
13	-30.0	-10.7	19.3	1.7	1,478,819	1.48
14	-11.7	-5.2	6.5	1.2	1,184,958	1.18
15	-58.7	-15.9	42.8	2.1	1,232,925	1.23
Average^{+}	35.6	12.4	23.3	2.5	2,150,603	2.2
Average^{-}	-33.3	-9.8	23.6	2.3	1,828,582	1.8

Table 17. SM computational results under shear, at varying strain rate. The varying strain rate is shown above separate tables, and the average of the results are shown below the data. The element number depicts the fibre count and was used as an ID number.

Shear – 1 Hz						
Element Number	**Original Fibre Angle [°]**	**Final Fibre Angle [°]**	**Change in angle [°]**	**Strain ε [-]**	**Normal Stress σ [Pa]**	**Normal Stress σ [MPa]**
1	57.8	77.9	20.1	1.5	690,333	0.69
2	-26.6	69.1	95.7	1.5	623,457	0.62
3	-25.6	50.4	76.0	0.4	329,197	0.33
4	-34.0	69.2	103.2	1.3	766,346	0.77
5	-11.5	61.6	73.1	1.1	199,789	0.20
6	-30.2	44.8	75.0	0.2	342,401	0.34
7	13.2	78.7	65.5	4.0	532,143	0.53
8	-56.1	64.7	120.8	0.3	834,000	0.83
9	-43.7	80.7	124.4	3.5	1,757,719	1.76
10	-46.4	70.4	116.8	1.1	964,504	0.96
11	-25.6	71.8	97.4	1.9	685,981	0.69
12	35.9	70.0	34.1	1.4	481,586	0.48
13	-30.0	55.9	85.9	0.5	444,405	0.44
14	-11.7	47.2	58.9	0.4	127,257	0.13
15	-58.7	72.2	131.0	0.7	1,058,154	1.06
Average^{+}	35.6	75.5	39.9	2.3	568,021	0.6
Average^{-}	-33.3	63.2	96.5	1.1	677,768	0.7
10 Hz						
Element Number	**Original Fibre Angle [°]**	**Final Fibre Angle [°]**	**Change in angle [°]**	**Strain ε [-]**	**Normal Stress σ [Pa]**	**Normal Stress σ [MPa]**
1	57.8	77.9	20.1	1.5	980,273	0.98
2	-26.6	69.1	95.7	1.5	885,309	0.89
3	-25.6	50.4	76.0	0.4	467,460	0.47
4	-34.0	69.2	103.2	1.3	1,088,212	1.09
5	-11.5	61.6	73.1	1.1	283,700	0.28
6	-30.2	44.8	75.0	0.2	486,209	0.49
7	13.2	78.7	65.5	4.0	755,642	0.76
8	-56.1	64.7	120.8	0.3	1,184,280	1.18
9	-43.7	80.7	124.4	3.5	2,495,960	2.50
10	-46.4	70.4	116.8	1.1	1,369,596	1.37

11	-25.6	71.8	97.4	1.9	974,093	0.97
12	35.9	70.0	34.1	1.4	683,851	0.68
13	-30.0	55.9	85.9	0.5	631,055	0.63
14	-11.7	47.2	58.9	0.4	180,705	0.18
15	-58.7	72.2	131.0	0.7	1,502,579	1.50
Average^{+}	35.6	75.5	39.9	2.3	806,589	0.8
Average^{-}	-33.3	63.2	96.5	1.1	962,430	1.0
100 Hz						
Element Number	**Original Fibre Angle [°]**	**Final Fibre Angle [°]**	**Change in angle [°]**	**Strain ε [-]**	**Normal Stress σ [Pa]**	**Normal Stress σ [MPa]**
1	57.8	77.9	20.1	1.5	1,394,473	1.39
2	-26.6	69.1	95.7	1.5	1,259,384	1.26
3	-25.6	50.4	76.0	0.4	664,979	0.66
4	-34.0	69.2	103.2	1.3	1,548,019	1.55
5	-11.5	61.6	73.1	1.1	403,573	0.40
6	-30.2	44.8	75.0	0.2	691,650	0.69
7	13.2	78.7	65.5	4.0	1,074,928	1.07
8	-56.1	64.7	120.8	0.3	1,684,679	1.68
9	-43.7	80.7	124.4	3.5	3,550,591	3.55
10	-46.4	70.4	116.8	1.1	1,948,299	1.95
11	-25.6	71.8	97.4	1.9	1,385,682	1.39
12	35.9	70.0	34.1	1.4	972,803	0.97
13	-30.0	55.9	85.9	0.5	897,697	0.90
14	-11.7	47.2	58.9	0.4	257,059	0.26
15	-58.7	72.2	131.0	0.7	2,137,471	2.14
Average^{+}	35.6	75.5	39.9	2.3	1,147,401	1.1
Average^{-}	-33.3	63.2	96.5	1.1	1,369,090	1.4

B.2 Ideal Model Load Results

Table 18. Applied load results at each node of the IM undergoing tension, at different strain rates. Each node has an x- and y- force component. The total forces in the x- and y-directions were determined.

Tension						
Node Number	**Element Number**	**x- or y-Direction**	**Applied Displacement [μm]**	**Forces (1 Hz) [N]**	**Forces (10 Hz) [N]**	**Forces (100 Hz) [N]**
1	**1**	**x**	0	0	0	0
		y	0	0	0	0
2		**x**	90.70	5.49E-07	8.12E-07	1.05E-06
		y	0	5.49E-07	8.12E-07	1.05E-06
3	**2**	**x**	0	0	0	0
		y	0	0	0	0
4		**x**	90.7	5.49E-07	8.12E-07	1.05E-06
		y	0	5.49E-07	8.12E-07	1.05E-06
5	**3**	**x**	0	0	0	0
		y	0	0	0	0
6		**x**	90.7	5.49E-07	8.12E-07	1.05E-06
		y	0	5.49E-07	8.12E-07	1.05E-06
7	**4**	**x**	0	0	0	0
		y	0	0	0	0
8		**x**	90.7	5.49E-07	8.12E-07	1.05E-06
		y	0	5.49E-07	8.12E-07	1.05E-06
9	**5**	**x**	0	0	0	0
		y	0	0	0	0
10		**x**	90.7	5.49E-07	8.12E-07	1.05E-06
		y	0	5.49E-07	8.12E-07	1.05E-06
11	**6**	**x**	0	0	0	0
		y	0	0	0	0
12		**x**	90.7	5.49E-07	8.12E-07	1.05E-06
		y	0	5.49E-07	8.12E-07	1.05E-06
13	**7**	**x**	0	0	0	0
		y	0	0	0	0
14		**x**	90.7	5.49E-07	8.12E-07	1.05E-06
		y	0	5.49E-07	8.12E-07	1.05E-06
15	**8**	**x**	0	0	0	0
		y	0	0	0	0
16		**x**	90.7	5.49E-07	8.12E-07	1.05E-06
		y	0	5.49E-07	8.12E-07	1.05E-06

17	**9**	**x**	0	0	0	0
		y	0	0	0	0
18		**x**	90.7	5.49E-07	8.12E-07	1.05E-06
		y	0	5.49E-07	8.12E-07	1.05E-06
19	**10**	**x**	0	0	0	0
		y	0	0	0	0
20		**x**	90.7	5.49E-07	8.12E-07	1.05E-06
		y	0	5.49E-07	8.12E-07	1.05E-06
21	**11**	**x**	0	0	0	0
		y	0	0	0	0
22		**x**	90.7	5.49E-07	8.12E-07	1.05E-06
		y	0	5.49E-07	8.12E-07	1.05E-06
23	**12**	**x**	0	0	0	0
		y	0	0	0	0
24		**x**	90.7	5.49E-07	8.12E-07	1.05E-06
		y	0	-5.49E-07	-8.12E-07	-1.05E-06
25	**13**	**x**	0	0	0	0
		y	0	0	0	0
26		**x**	90.7	5.49E-07	8.12E-07	1.05E-06
		y	0	-5.49E-07	-8.12E-07	-1.05E-06
27	**14**	**x**	0	0	0	0
		y	0	0	0	0
28		**x**	90.7	5.49E-07	8.12E-07	1.05E-06
		y	0	-5.49E-07	-8.12E-07	-1.05E-06
29	**15**	**x**	0	0	0	0
		y	0	0	0	0
30		**x**	90.7	5.49E-07	8.12E-07	1.05E-06
		y	0	-5.49E-07	-8.12E-07	-1.05E-06
31	**16**	**x**	0	0	0	0
		y	0	0	0	0
32		**x**	90.7	5.49E-07	8.12E-07	1.05E-06
		y	0	-5.49E-07	-8.12E-07	-1.05E-06
33	**17**	**x**	0	0	0	0
		y	0	0	0	0
34		**x**	90.7	5.49E-07	8.12E-07	1.05E-06
		y	0	-5.49E-07	-8.12E-07	-1.05E-06
35	**18**	**x**	0	0	0	0
		y	0	0	0	0
36		**x**	90.7	5.49E-07	8.12E-07	1.05E-06
		y	0	-5.49E-07	-8.12E-07	-1.05E-06
37	**19**	**x**	0	0	0	0

		y	0	0	0	0
38		**x**	90.7	5.49E-07	8.12E-07	1.05E-06
		y	0	-5.49E-07	-8.12E-07	-1.05E-06
39	**20**	**x**	0	0	0	0
		y	0	0	0	0
40		**x**	90.7	5.49E-07	8.12E-07	1.05E-06
		y	0	-5.49E-07	-8.12E-07	-1.05E-06
41	**21**	**x**	0	0	0	0
		y	0	0	0	0
42		**x**	90.7	5.49E-07	8.12E-07	1.05E-06
		y	0	-5.49E-07	-8.12E-07	-1.05E-06
43	**22**	**x**	0	0	0	0
		y	0	0	0	0
44		**x**	90.7	5.49E-07	8.12E-07	1.05E-06
		y	0	-5.49E-07	-8.12E-07	-1.05E-06
Summation of x- and y-values		**x**	-	1.21E-05	1.79E-05	2.32E-05
		y	-	0	0	0

Table 19. Applied load results at each node of the IM undergoing shear, at different strain rates. Each node has an x- and y- force component. The total forces in the x- and y-directions were determined.

Shear						
Node Number	**Element Number**	**x- or y-Direction**	**Applied Displacement [µm]**	**Forces (1 Hz) [N]**	**Forces (10 Hz) [N]**	**Forces (100 Hz) [N]**
1	**1**	**x**	0	0	0	0
		y	0	0	0	0
2		**x**	0	5.49E-07	7.79E-07	1.11E-06
		y	90.70	5.49E-07	7.79E-07	1.11E-06
3	**2**	**x**	0	0	0	0
		y	0	0	0	0
4		**x**	0	5.49E-07	7.79E-07	1.11E-06
		y	90.70	5.49E-07	7.79E-07	1.11E-06
5	**3**	**x**	0	0	0	0
		y	0	0	0	0
6		**x**	0	5.49E-07	7.79E-07	1.11E-06
		y	90.70	5.49E-07	7.79E-07	1.11E-06
7	**4**	**x**	0	0	0	0
		y	0	0	0	0
8		**x**	0	5.49E-07	7.79E-07	1.11E-06

		y	90.70	5.49E-07	7.79E-07	1.11E-06
9	**5**	**x**	0	0	0	0
		y	0	0	0	0
10		**x**	0	5.49E-07	7.79E-07	1.11E-06
		y	90.70	5.49E-07	7.79E-07	1.11E-06
11	**6**	**x**	0	0	0	0
		y	0	0	0	0
12		**x**	0	5.49E-07	7.79E-07	1.11E-06
		y	90.70	5.49E-07	7.79E-07	1.11E-06
13	**7**	**x**	0	0	0	0
		y	0	0	0	0
14		**x**	0	5.49E-07	7.79E-07	1.11E-06
		y	90.70	5.49E-07	7.79E-07	1.11E-06
15	**8**	**x**	0	0	0	0
		y	0	0	0	0
16		**x**	0	5.49E-07	7.79E-07	1.11E-06
		y	90.70	5.49E-07	7.79E-07	1.11E-06
17	**9**	**x**	0	0	0	0
		y	0	0	0	0
18		**x**	0	5.49E-07	7.79E-07	1.11E-06
		y	90.70	5.49E-07	7.79E-07	1.11E-06
19	**10**	**x**	0	0	0	0
		y	0	0	0	0
20		**x**	0	5.49E-07	7.79E-07	1.11E-06
		y	90.70	5.49E-07	7.79E-07	1.11E-06
21	**11**	**x**	0	0	0	0
		y	0	0	0	0
22		**x**	0	5.49E-07	7.79E-07	1.11E-06
		y	90.70	5.49E-07	7.79E-07	1.11E-06
23	**12**	**x**	0	0	0	0
		y	0	0	0	0
24		**x**	0	-5.49E-07	-7.79E-07	-1.11E-06
		y	90.70	5.49E-07	7.79E-07	1.11E-06
25	**13**	**x**	0	0	0	0
		y	0	0	0	0
26		**x**	0	-5.49E-07	-7.79E-07	-1.11E-06
		y	90.70	5.49E-07	7.79E-07	1.11E-06
27	**14**	**x**	0	0	0	0
		y	0	0	0	0
28		**x**	0	-5.49E-07	-7.79E-07	-1.11E-06
		y	90.70	5.49E-07	7.79E-07	1.11E-06

29	**15**	**x**	0	0	0	0
		y	0	0	0	0
30		**x**	0	-5.49E-07	-7.79E-07	-1.11E-06
		y	90.70	5.49E-07	7.79E-07	1.11E-06
31	**16**	**x**	0	0	0	0
		y	0	0	0	0
32		**x**	0	-5.49E-07	-7.79E-07	-1.11E-06
		y	90.70	5.49E-07	7.79E-07	1.11E-06
33	**17**	**x**	0	0	0	0
		y	0	0	0	0
34		**x**	0	-5.49E-07	-7.79E-07	-1.11E-06
		y	90.70	5.49E-07	7.79E-07	1.11E-06
35	**18**	**x**	0	0	0	0
		y	0	0	0	0
36		**x**	0	-5.49E-07	-7.79E-07	-1.11E-06
		y	90.70	5.49E-07	7.79E-07	1.11E-06
37	**19**	**x**	0	0	0	0
		y	0	0	0	0
38		**x**	0	-5.49E-07	-7.79E-07	-1.11E-06
		y	90.70	5.49E-07	7.79E-07	1.11E-06
39	**20**	**x**	0	0	0	0
		y	0	0	0	0
40		**x**	0	-5.49E-07	-7.79E-07	-1.11E-06
		y	90.70	5.49E-07	7.79E-07	1.11E-06
41	**21**	**x**	0	0	0	0
		y	0	0	0	0
42		**x**	0	-5.49E-07	-7.79E-07	-1.11E-06
		y	90.70	5.49E-07	7.79E-07	1.11E-06
43	**22**	**x**	0	0	0	0
		y	0	0	0	0
44		**x**	0	-5.49E-07	-7.79E-07	-1.11E-06
		y	90.70	5.49E-07	7.79E-07	1.11E-06
Summation of x- and y-values		**x**	-	0	0	0
		y	-	1.21E-05	1.71E-05	2.44E-05

B.3 Ideal Model with Diagonal Fibre Load Results

Table 20. Applied load results at each node of the IMD undergoing tension, at different strain rates. Each node has an x- and y- force component. The total forces in the x- and y-directions were determined.

Tension						
Node Number	**Element Number**	**x- or y-Direction**	**Applied Displacement [µm]**	**Forces (1 Hz) [N]**	**Forces (10 Hz) [N]**	**Forces (100 Hz) [N]**
1	**1 23**	**x**	0	0	0	0
		y	0	0	0	0
2		**x**	0	5.49E-07	8.12E-07	1.05E-06
		y	90.70	5.49E-07	8.12E-07	1.05E-06
3	**2**	**x**	0	0	0	0
		y	0	0	0	0
4		**x**	0	5.49E-07	8.12E-07	1.05E-06
		y	90.70	5.49E-07	8.12E-07	1.05E-06
5	**3**	**x**	0	0	0	0
		y	0	0	0	0
6		**x**	0	5.49E-07	8.12E-07	1.05E-06
		y	90.70	5.49E-07	8.12E-07	1.05E-06
7	**4**	**x**	0	0	0	0
		y	0	0	0	0
8		**x**	0	5.49E-07	8.12E-07	1.05E-06
		y	90.70	5.49E-07	8.12E-07	1.05E-06
9	**5**	**x**	0	0	0	0
		y	0	0	0	0
10		**x**	0	5.49E-07	8.12E-07	1.05E-06
		y	90.70	5.49E-07	8.12E-07	1.05E-06
11	**6**	**x**	0	0	0	0
		y	0	0	0	0
12		**x**	0	5.49E-07	8.12E-07	1.05E-06
		y	90.70	5.49E-07	8.12E-07	1.05E-06
13	**7**	**x**	0	0	0	0
		y	0	0	0	0
14		**x**	0	5.49E-07	8.12E-07	1.05E-06
		y	90.70	5.49E-07	8.12E-07	1.05E-06
15	**8**	**x**	0	0	0	0
		y	0	0	0	0
16		**x**	0	5.49E-07	8.12E-07	1.05E-06
		y	90.70	5.49E-07	8.12E-07	1.05E-06

17	**9**	**x**	0	0	0	0
		y	0	0	0	0
18		**x**	0	5.49E-07	8.12E-07	1.05E-06
		y	90.70	5.49E-07	8.12E-07	1.05E-06
19	**10**	**x**	0	0	0	0
		y	0	0	0	0
20		**x**	0	5.49E-07	8.12E-07	1.05E-06
		y	90.70	5.49E-07	8.12E-07	1.05E-06
21	**11**	**x**	0	0	0	0
		y	0	0	0	0
22	**23**	**x**	0	7.04E-07	1.04E-06	1.35E-06
		y	90.70	8.45E-07	1.25E-06	1.62E-06
23	**12**	**x**	0	0	0	0
		y	0	0	0	0
24		**x**	0	5.49E-07	8.12E-07	1.05E-06
		y	90.70	-5.49E-07	-8.12E-07	-1.05E-06
25	**13**	**x**	0	0	0	0
		y	0	0	0	0
26		**x**	0	5.49E-07	8.12E-07	1.05E-06
		y	90.70	-5.49E-07	-8.12E-07	-1.05E-06
27	**14**	**x**	0	0	0	0
		y	0	0	0	0
28		**x**	0	5.49E-07	8.12E-07	1.05E-06
		y	90.70	-5.49E-07	-8.12E-07	-1.05E-06
29	**15**	**x**	0	0	0	0
		y	0	0	0	0
30		**x**	0	5.49E-07	8.12E-07	1.05E-06
		y	90.70	-5.49E-07	-8.12E-07	-1.05E-06
31	**16**	**x**	0	0	0	0
		y	0	0	0	0
32		**x**	0	5.49E-07	8.12E-07	1.05E-06
		y	90.70	-5.49E-07	-8.12E-07	-1.05E-06
33	**17**	**x**	0	0	0	0
		y	0	0	0	0
34		**x**	0	5.49E-07	8.12E-07	1.05E-06
		y	90.70	-5.49E-07	-8.12E-07	-1.05E-06
35	**18**	**x**	0	0	0	0
		y	0	0	0	0
36		**x**	0	5.49E-07	8.12E-07	1.05E-06
		y	90.70	-5.49E-07	-8.12E-07	-1.05E-06
37	**19**	**x**	0	0	0	0

		y	0	0	0	0
38		**x**	0	5.49E-07	8.12E-07	1.05E-06
		y	90.70	-5.49E-07	-8.12E-07	-1.05E-06
39	**20**	**x**	0	0	0	0
		y	0	0	0	0
40		**x**	0	5.49E-07	8.12E-07	1.05E-06
		y	90.70	-5.49E-07	-8.12E-07	-1.05E-06
41	**21**	**x**	0	0	0	0
		y	0	0	0	0
42		**x**	0	5.49E-07	8.12E-07	1.05E-06
		y	90.70	-5.49E-07	-8.12E-07	-1.05E-06
43	**22**	**x**	0	0	0	0
		y	0	0	0	0
44		**x**	0	5.49E-07	8.12E-07	1.05E-06
		y	90.70	-5.49E-07	-8.12E-07	-1.05E-06
Summation of x- and y-values		**x**	-	1.22E-05	1.81E-05	2.35E-05
		y	-	0	0	0

Table 21. Applied load results at each node of the IMD undergoing shear, at different strain rates. Each node has an x- and y- force component. The total forces in the x- and y-directions were determined.

Shear						
Node Number	**Element Number**	**x- or y-Direction**	**Applied Displacement [µm]**	**Forces (1 Hz) [N]**	**Forces (10 Hz) [N]**	**Forces (100 Hz) [N]**
1	**1 23**	**x**	0	0	0	0
		y	0	0	0	0
2		**x**	0	5.49E-07	7.79E-07	1.11E-06
		y	90.70	5.49E-07	7.79E-07	1.11E-06
3	**2**	**x**	0	0	0	0
		y	0	0	0	0
4		**x**	0	5.49E-07	7.79E-07	1.11E-06
		y	90.70	5.49E-07	7.79E-07	1.11E-06
5	**3**	**x**	0	0	0	0
		y	0	0	0	0
6		**x**	0	5.49E-07	7.79E-07	1.11E-06
		y	90.70	5.49E-07	7.79E-07	1.11E-06
7	**4**	**x**	0	0	0	0
		y	0	0	0	0

8		**x**	0	5.49E-07	7.79E-07	1.11E-06
		y	90.70	5.49E-07	7.79E-07	1.11E-06
9	**5**	**x**	0	0	0	0
		y	0	0	0	0
10		**x**	0	5.49E-07	7.79E-07	1.11E-06
		y	90.70	5.49E-07	7.79E-07	1.11E-06
11	**6**	**x**	0	0	0	0
		y	0	0	0	0
12		**x**	0	5.49E-07	7.79E-07	1.11E-06
		y	90.70	5.49E-07	7.79E-07	1.11E-06
13	**7**	**x**	0	0	0	0
		y	0	0	0	0
14		**x**	0	5.49E-07	7.79E-07	1.11E-06
		y	90.70	5.49E-07	7.79E-07	1.11E-06
15	**8**	**x**	0	0	0	0
		y	0	0	0	0
16		**x**	0	5.49E-07	7.79E-07	1.11E-06
		y	90.70	5.49E-07	7.79E-07	1.11E-06
17	**9**	**x**	0	0	0	0
		y	0	0	0	0
18		**x**	0	5.49E-07	7.79E-07	1.11E-06
		y	90.70	5.49E-07	7.79E-07	1.11E-06
19	**10**	**x**	0	0	0	0
		y	0	0	0	0
20		**x**	0	5.49E-07	7.79E-07	1.11E-06
		y	90.70	5.49E-07	7.79E-07	1.11E-06
21	**11**	**x**	0	0	0	0
		y	0	0	0	0
22	**23**	**x**	0	8.45E-07	1.20E-06	1.71E-06
		y	90.70	1.11E-06	1.58E-06	2.25E-06
23	**12**	**x**	0	0	0	0
		y	0	0	0	0
24		**x**	0	-5.49E-07	-7.79E-07	-1.11E-06
		y	90.70	5.49E-07	7.79E-07	1.11E-06
25	**13**	**x**	0	0	0	0
		y	0	0	0	0
26		**x**	0	-5.49E-07	-7.79E-07	-1.11E-06
		y	90.70	5.49E-07	7.79E-07	1.11E-06
27	**14**	**x**	0	0	0	0
		y	0	0	0	0
28		**x**	0	-5.49E-07	-7.79E-07	-1.11E-06

		y	90.70	5.49E-07	7.79E-07	1.11E-06
29	**15**	**x**	0	0	0	0
		y	0	0	0	0
30		**x**	0	-5.49E-07	-7.79E-07	-1.11E-06
		y	90.70	5.49E-07	7.79E-07	1.11E-06
31	**16**	**x**	0	0	0	0
		y	0	0	0	0
32		**x**	0	-5.49E-07	-7.79E-07	-1.11E-06
		y	90.70	5.49E-07	7.79E-07	1.11E-06
33	**17**	**x**	0	0	0	0
		y	0	0	0	0
34		**x**	0	-5.49E-07	-7.79E-07	-1.11E-06
		y	90.70	5.49E-07	7.79E-07	1.11E-06
35	**18**	**x**	0	0	0	0
		y	0	0	0	0
36		**x**	0	-5.49E-07	-7.79E-07	-1.11E-06
		y	90.70	5.49E-07	7.79E-07	1.11E-06
37	**19**	**x**	0	0	0	0
		y	0	0	0	0
38		**x**	0	-5.49E-07	-7.79E-07	-1.11E-06
		y	90.70	5.49E-07	7.79E-07	1.11E-06
39	**20**	**x**	0	0	0	0
		y	0	0	0	0
40		**x**	0	-5.49E-07	-7.79E-07	-1.11E-06
		y	90.70	5.49E-07	7.79E-07	1.11E-06
41	**21**	**x**	0	0	0	0
		y	0	0	0	0
42		**x**	0	-5.49E-07	-7.79E-07	-1.11E-06
		y	90.70	5.49E-07	7.79E-07	1.11E-06
43	**22**	**x**	0	0	0	0
		y	0	0	0	0
44		**x**	0	-5.49E-07	-7.79E-07	-1.11E-06
		y	90.70	5.49E-07	7.79E-07	1.11E-06
Summation of x- and y-values		**x**	-	0	0	0
		y	-	1.26E-05	1.79E-05	2.55E-05

B.4 Specimen Model Load Results

Table 22. Applied load results at each node of the SM undergoing shear, at different strain rates. Each node has an x- and y- force component. The total forces in the x- and y-directions were determined.

Tension					
Node Number	**x- or y-Direction**	**Applied Displacement [μm]**	**Forces (1 Hz) [N]**	**Forces (10 Hz) [N]**	**Forces (100 Hz) [N]**
1	**x**	0	0	0	0
	y	0	0	0	0
2	**x**	2.53E-05	2.01E-07	2.98E-07	3.86E-07
	y	0	3.19E-07	4.72E-07	6.12E-07
3	**x**	0	0	0	0
	y	0	0	0	0
4	**x**	2.53E-05	9.66E-07	1.43E-06	1.86E-06
	y	0	-4.83E-07	-7.15E-07	-9.27E-07
5	**x**	0	0	0	0
	y	0	0	0	0
6	**x**	2.53E-05	5.36E-07	7.94E-07	1.03E-06
	y	0	-2.57E-07	-3.80E-07	-4.94E-07
7	**x**	0	0	0	0
	y	0	0	0	0
8	**x**	2.53E-05	8.17E-07	1.21E-06	1.57E-06
	y	0	-5.50E-07	-8.15E-07	-1.06E-06
9	**x**	0	0	0	0
	y	0	0	0	0
10	**x**	2.53E-05	8.37E-07	1.24E-06	1.61E-06
	y	0	-1.70E-07	-2.51E-07	-3.26E-07
11	**x**	2.53E-05	4.40E-07	6.51E-07	8.45E-07
	y	0	-2.56E-07	-3.79E-07	-4.92E-07
12	**x**	0	0	0	0
	y	0	0	0	0
13	**x**	2.53E-05	1.91E-06	2.82E-06	3.66E-06
	y	0	4.49E-07	6.64E-07	8.61E-07
14	**x**	0	0	0	0
	y	0	0	0	0
15	**x**	2.53E-05	2.70E-07	4.00E-07	5.19E-07
	y	0	-4.03E-07	-5.96E-07	-7.73E-07
16	**x**	0	0	0	0

	y	0	0	0	0
17	**x**	2.53E-05	1.15E-06	1.70E-06	2.21E-06
	y	0	-1.10E-06	-1.63E-06	-2.11E-06
18	**x**	0	0	0	0
	y	0	0	0	0
19	**x**	2.53E-05	5.50E-07	8.13E-07	1.06E-06
	y	0	-5.76E-07	-8.53E-07	-1.11E-06
20	**x**	2.53E-05	1.12E-06	1.66E-06	2.15E-06
	y	0	-5.36E-07	-7.93E-07	-1.03E-06
21	**x**	2.53E-05	4.66E-07	6.89E-07	8.94E-07
	y	0	3.38E-07	5.00E-07	6.48E-07
22	**x**	0	0	0	0
	y	0	0	0	0
23	**x**	2.53E-05	5.78E-07	8.55E-07	1.11E-06
	y	0	-3.33E-07	-4.93E-07	-6.40E-07
24	**x**	0	0	0	0
	y	0	0	0	0
25	**x**	2.53E-05	5.23E-07	7.75E-07	1.00E-06
	y	0	-1.08E-07	-1.60E-07	-2.07E-07
26	**x**	0	0	0	0
	y	0	0	0	0
27	**x**	2.53E-05	2.88E-07	4.27E-07	5.54E-07
	y	0	-4.75E-07	-7.04E-07	-9.13E-07
Summation of x- and y-values	**x**	-	1.06E-05	1.58E-05	2.04E-05
	y	-	0	0	0

Table 23. Applied and reaction load results at each node of the SM undergoing shear, at different strain rates. Each node has an x- and y- force component, which includes both applied and reaction load. The average force was determined from the forces corresponding to the applied displacement, in the y-direction.

Shear					
Node Number	**x- or y-Direction**	**Applied Displacement [µm]**	**Forces (1 Hz) [N]**	**Forces (10 Hz) [N]**	**Forces (100 Hz) [N]**
1	**x**	0	0	0	0
	y	0	0	0	0
2	**x**	0	3.19E-07	4.53E-07	6.44E-07
	y	25.34	5.06E-07	7.18E-07	1.02E-06
3	**x**	0	0	0	0

	y	0	0	0	0
4	**x**	0	-4.83E-07	-6.86E-07	-9.75E-07
	y	25.34	2.41E-07	3.43E-07	4.87E-07
5	**x**	0	0	0	0
	y	0	0	0	0
6	**x**	0	-2.57E-07	-3.65E-07	-5.19E-07
	y	25.34	1.23E-07	1.75E-07	2.49E-07
7	**x**	0	0	0	0
	y	0	0	0	0
8	**x**	0	-5.50E-07	-7.82E-07	-1.11E-06
	y	25.34	3.71E-07	5.26E-07	7.49E-07
9	**x**	0	0	0	0
	y	0	0	0	0
10	**x**	0	-1.70E-07	-2.41E-07	-3.42E-07
	y	25.34	3.44E-08	4.88E-08	6.94E-08
11	**x**	0	-2.56E-07	-3.64E-07	-5.18E-07
	y	25.34	1.49E-07	2.12E-07	3.01E-07
12	**x**	0	0	0	0
	y	0	0	0	0
13	**x**	0	4.49E-07	6.37E-07	9.06E-07
	y	25.34	1.06E-07	1.50E-07	2.13E-07
14	**x**	0	0	0	0
	y	0	0	0	0
15	**x**	0	-4.03E-07	-5.72E-07	-8.13E-07
	y	25.34	6.00E-07	8.51E-07	1.21E-06
16	**x**	0	0	0	0
	y	0	0	0	0
17	**x**	0	-1.10E-06	-1.56E-06	-2.22E-06
	y	25.34	1.05E-06	1.49E-06	2.12E-06
18	**x**	0	0	0	0
	y	0	0	0	0
19	**x**	0	-5.76E-07	-8.18E-07	-1.16E-06
	y	25.34	6.04E-07	8.58E-07	1.22E-06
20	**x**	0	-5.36E-07	-7.61E-07	-1.08E-06
	y	25.34	2.56E-07	3.64E-07	5.18E-07
21	**x**	0	3.38E-07	4.79E-07	6.82E-07
	y	25.34	2.45E-07	3.48E-07	4.94E-07
22	**x**	0	0	0	0
	y	0	0	0	0
23	**x**	0	-3.33E-07	-4.73E-07	-6.73E-07
	y	25.34	1.92E-07	2.73E-07	3.88E-07
24	**x**	0	0	0	0
	y	0	0	0	0

25	**x**	0	-1.08E-07	-1.53E-07	-2.18E-07
	y	25.34	2.23E-08	3.16E-08	4.50E-08
26	**x**	0	0	0	0
	y	0	0	0	0
27	**x**	0	-4.75E-07	-6.75E-07	-9.60E-07
	y	25.34	7.83E-07	1.11E-06	1.58E-06
Summation of x- and y-values	**x**	-	0	0	0
	y	-	5.28E-06	7.50E-06	1.07E-05

References

Bruehlmann, S. B., Rattner, J. B., Matyas, J. R., & Duncan, N. A. (2002). Regional variations in the cellular matrix of the annulus fibrosus of the intervertebral disc. *J Anat, 201*(2), 159-171.

Cramer, G. D., Bakkum, B. W., & Stathopoulos, P. C. Microscopic Anatomy of the Zygapophysial Joints, Intervertebral Discs, and Other Major Tissues of the Back. Retrieved from https://basicmedicalkey.com/microscopic-anatomy-of-the-zygapophysial-joints-intervertebral-discs-and-other-major-tissues-of-the-back/

Goel, V. K., Monroe, B. T., Gilbertson, L. G., & Brinckmann, P. (1995). Interlaminar shear stresses and laminae separation in a disc. Finite element analysis of the L3-L4 motion segment subjected to axial compressive loads. *Spine (Phila Pa 1976), 20*(6), 689-698.

Gregory, D. E., Veldhuis, J. H., Horst, C., Wayne Brodland, G., & Callaghan, J. P. (2011). Novel lap test determines the mechanics of delamination between annular lamellae of the intervertebral disc. *J Biomech, 44*(1), 97-102. doi:10.1016/j.jbiomech.2010.08.031

Han, S. K., Chen, C. W., Wierwille, J., Chen, Y., & Hsieh, A. H. (2015). Three dimensional mesoscale analysis of translamellar cross-bridge morphologies in the annulus fibrosus using optical coherence tomography. *J Orthop Res, 33*(3), 304-311. doi:10.1002/jor.22778

Iatridis, J. C., & ap Gwynn, I. (2004). Mechanisms for mechanical damage in the intervertebral disc annulus fibrosus. *J Biomech, 37*(8), 1165-1175. doi:10.1016/j.jbiomech.2003.12.026

Labus, K. M., Han, S. K., Hsieh, A. H., & Puttlitz, C. M. (2014). A computational model to describe the regional interlamellar shear of the annulus fibrosus. *J Biomech Eng, 136*(5), 051009. doi:10.1115/1.4027061

Mengoni, M., Luxmoore, B. J., Wijayathunga, V. N., Jones, A. C., Broom, N. D., & Wilcox, R. K. (2015). Derivation of inter-lamellar behaviour of the intervertebral disc annulus. *J Mech Behav Biomed Mater, 48*, 164-172. doi:10.1016/j.jmbbm.2015.03.028

Mengoni, M., Wijayathunga, V. N., Jones, A. C., & Wilcox, R. K. (2013). *Structural modelling of the annulus fibrosus-an anisotropic hyperelastic model approach at the lamellar level*. Paper presented at the 3rd International Conference on Mathematical and Computational Biomedical Engineering, Leeds.

Michalek, A. J., Buckley, M. R., Bonassar, L. J., Cohen, I., & Iatridis, J. C. (2009). Measurement of local strains in intervertebral disc anulus fibrosus tissue under dynamic shear: contributions of matrix fiber orientation and elastin content. *J Biomech, 42*(14), 2279-2285. doi:10.1016/j.jbiomech.2009.06.047

Nerurkar, N. L., Elliott, D. M., & Mauck, R. L. (2010). Mechanical design criteria for intervertebral disc tissue engineering. *J Biomech, 43*(6), 1017-1030. doi:10.1016/j.jbiomech.2009.12.001

Nerurkar, N. L., Mauck, R. L., & Elliott, D. M. (2011). Modeling interlamellar interactions in angle-ply biologic laminates for annulus fibrosus tissue engineering. *Biomech Model Mechanobiol, 10*(6), 973-984. doi:10.1007/s10237-011-0288-0

Schollum, M. L., Robertson, P. A., & Broom, N. D. (2008). ISSLS prize winner: microstructure and mechanical disruption of the lumbar disc annulus: part I: a microscopic investigation of the translamellar bridging network. *Spine (Phila Pa 1976), 33*(25), 2702-2710. doi:10.1097/BRS.0b013e31817bb92c

Schollum, M. L., Robertson, P. A., & Broom, N. D. (2009). A microstructural investigation of intervertebral disc lamellar connectivity: detailed analysis of the translamellar bridges. *J Anat, 214*(6), 805-816. doi:10.1111/j.1469-7580.2009.01076.x

Smith, L. J., Byers, S., Costi, J. J., & Fazzalari, N. L. (2008). Elastic fibers enhance the mechanical integrity of the human lumbar anulus fibrosus in the radial direction. *Ann Biomed Eng, 36*(2), 214-223. doi:10.1007/s10439-007-9421-8

Smith, L. J., & Fazzalari, N. L. (2009). The elastic fibre network of the human lumbar anulus fibrosus: architecture, mechanical function and potential role in the progression of intervertebral disc degeneration. *Eur Spine J, 18*(4), 439-448. doi:10.1007/s00586-009-0918-8

Tavakoli, J., & Costi, J. J. (2016). *Development of a rapid matrix digestion technique for ultrastructural analysis of elastic fibers in the intervertebral disc.* Flinders University,

Tavakoli, J., Elliott, D. M., & Costi, J. J. (2016). Structure and mechanical function of the inter-lamellar matrix of the annulus fibrosus in the disc. *J Orthop Res, 34*(8), 1307-1315. doi:10.1002/jor.23306

Tavakoli, J., Elliott, D. M., & Costi, J. J. (2017a). *New findings confirm the contribution of the inter-lamellar matrix to the mechanical properties of disc annulus fibrosus in radial and circumferential directions*. (Unpublished).

Tavakoli, J., Elliott, D. M., & Costi, J. J. (2017b). The ultra-structural organization of the elastic network in the intra- and inter-lamellar matrix of the intervertebral disc. *Acta Biomater, 58*, 269-277. doi:10.1016/j.actbio.2017.05.036

The MathWorks, I. (R2016a). Matlab and Statistics Toolbox Release R2016a Natick, Massachusetts, United States.

Ugural, A. C., & Fenster, S. K. (2011). *Advanced mechanics of materials and applied elasticity*. Pearson Education.

Vergari, C., Mansfield, J., Meakin, J. R., & Winlove, P. C. (2016). Lamellar and fibre bundle mechanics of the annulus fibrosus in bovine intervertebral disc. *Acta Biomater, 37*, 14-20. doi:10.1016/j.actbio.2016.04.002

Yu, J., Schollum, M. L., Wade, K. R., Broom, N. D., & Urban, J. P. (2015). ISSLS Prize Winner: A Detailed Examination of the Elastic Network Leads to a New Understanding of Annulus Fibrosus Organization. *Spine (Phila Pa 1976), 40*(15), 1149-1157. doi:10.1097/BRS.0000000000000943